AGU PUBLICATIONS

Space Weather

RESEARCH ARTICLE
10.1002/2016SW001529

Special Section:
NASA's Living With a Star: Geomagnetically Induced Currents

Key Points:
- Presents the first comparison between observed field-aligned currents and models previously evaluated for space weather operational use
- The model and observed integrated currents are well correlated, but the ratio between them ranges from 1/3 to 3
- The 2-D current densities are weakly correlated with observations implying significant areas for improvements in the models

Correspondence to:
B. J. Anderson,
brian.anderson@jhuapl.edu

Citation:
Anderson, B. J., H. Korth, D. T. Welling, V. G. Merkin, M. J. Wiltberger, J. Raeder, R. J. Barnes, C. L. Waters, A. A. Pulkkinen, and L. Rastaetter (2017), Comparison of predictive estimates of high-latitude electrodynamics with observations of global-scale Birkeland currents, *Space Weather*, *15*, 352–373, doi:10.1002/2016SW001529.

Received 3 SEP 2016
Accepted 22 DEC 2016
Accepted article online 23 DEC 2016
Published online 13 FEB 2017

Comparison of predictive estimates of high-latitude electrodynamics with observations of global-scale Birkeland currents

Brian J. Anderson[1], Haje Korth[1], Daniel T. Welling[2], Viacheslav G. Merkin[1], Michael J. Wiltberger[3], Joachim Raeder[4], Robin J. Barnes[1], Colin L. Waters[5], Antti A. Pulkkinen[6], and Lutz Rastaetter[6]

[1]The Johns Hopkins University Applied Physics Laboratory, Laurel, Maryland, USA, [2]Department of Climate and Space Sciences and Engineering, University of Michigan, Ann Arbor, Michigan, USA, [3]University Center for Atmospheric Research, University of Colorado Boulder, Boulder, Colorado, USA, [4]Physics Department & Space Science Center, University of New Hampshire, Durham, New Hampshire, USA, [5]Department of Mathematical and Physical Sciences, University of Newcastle, Newcastle, New South Wales, Australia, [6]NASA Goddard Space Flight Center, Greenbelt, Maryland, USA

Abstract Two of the geomagnetic storms for the Space Weather Prediction Center Geospace Environment Modeling challenge occurred after data were first acquired by the Active Magnetosphere and Planetary Electrodynamics Response Experiment (AMPERE). We compare Birkeland currents from AMPERE with predictions from four models for the 4–5 April 2010 and 5–6 August 2011 storms. The four models are the Weimer (2005b) field-aligned current statistical model, the Lyon-Fedder-Mobarry magnetohydrodynamic (MHD) simulation, the Open Global Geospace Circulation Model MHD simulation, and the Space Weather Modeling Framework MHD simulation. The MHD simulations were run as described in Pulkkinen et al. (2013) and the results obtained from the Community Coordinated Modeling Center. The total radial Birkeland current, I_{Total}, and the distribution of radial current density, J_r, for all models are compared with AMPERE results. While the total currents are well correlated, the quantitative agreement varies considerably. The J_r distributions reveal discrepancies between the models and observations related to the latitude distribution, morphologies, and lack of nightside current systems in the models. The results motivate enhancing the simulations first by increasing the simulation resolution and then by examining the relative merits of implementing more sophisticated ionospheric conductance models, including ionospheric outflows or other omitted physical processes. Some aspects of the system, including substorm timing and location, may remain challenging to simulate, implying a continuing need for real-time specification.

1. Introduction

It is now recognized that extreme events may present significant threats to modern utility power, communications, and navigation technology infrastructures [*Tsurutani and Lakhina*, 2014; *Love et al.*, 2015; *Curto et al.*, 2016; *Pulkkinen et al.*, 2017]. Indeed, there is a societal imperative to quantitatively understand the likely geospace consequences of such events to provide reliable guidance for government policy, mitigation planning, and technology development [*National Research Council*, 2008; *North American Electric Reliability Corporation GMD Task Force*, 2012; *National Science and Technology Council*, 2015a; *National Science and Technology Council*, 2015b]. In the absence of modern observations during extreme storms, assessment of their effects relies substantially on physics-based simulations of the magnetosphere-ionosphere (M-I) system response. System nonlinearities, feedback, and saturation effects imply that extrapolation of statistical models is potentially problematic [*Siscoe et al.*, 2004; *Muhlbacher et al.*, 2005; *Partamies et al.*, 2009; *DeJong et al.*, 2009; *Glocer et al.*, 2009; *Wiltberger et al.*, 2010; *Brambles et al.*, 2011; *Ouellette et al.*, 2013; *Cosgrove et al.*, 2014]. Physical simulations are therefore arguably the best technique to predict the dynamics of extreme events. However, reliable numerical simulations of extreme events are challenging because these events correspond to conditions beyond the realm of validity for the existing simulation codes [cf. *Ngwira et al.*, 2014]. To guide further development, we need to validate the simulations against the best available observations for the most intense events for which data are available.

Validation work for multiple models has been performed as part of the effort to select a first-generation operational space weather prediction simulation. Six geomagnetic storms were used to evaluate the performance of three global, physics-based, magnetohydrodynamic (MHD) simulations of Earth's magnetosphere [cf. *Pulkkinen et al*., 2013; *Ngwira et al*., 2014]. The metrics used to date have been a subset of ground magnetometer records motivated for a number of reasons including the availability of the data and the relationship to space weather effects on the ground, particularly ground induced currents (GICs) [cf. *Pulkkinen et al*., 2013; *Welling et al*., 2016].

Since these analyses, global-scale observations of the Birkeland currents have become available from the Active Magnetosphere and Planetary Electrodynamics Response Experiment (AMPERE). Data from AMPERE were released in 2012, span 1 January 2010 to the present, and provide nearly continuous coverage of large-scale Birkeland currents in both hemispheres [cf. *Anderson et al*., 2000; *Waters et al*., 2001; *Clausen et al*., 2012; *Anderson et al*., 2014]. Using AMPERE data, the Assimilative Mapping of Ionospheric Electrodynamics has been applied to a number of geomagnetic storms [cf. *Matsuo et al*., 2015]. *Wilder et al*. [2012] obtained dramatic differences in ionospheric Joule heating rates and distributions relative to assimilations using only ground magnetometer, radar, and operational low Earth orbit satellite observations. *Marsal et al*. [2012] achieved considerable success in reproducing ground magnetometer observations, and *Lu et al*. [2014] found remarkable agreement between simulated and observed neutral density storm time dynamics.

For comparison with the Space Weather Prediction Center (SWPC) Geospace Environment Modeling (GEM) challenge events, we use the compilation of MHD simulation results for the two GEM challenge events for which AMPERE data are available. We compare the simulated and observed Birkeland currents for the 5 April 2010 (Event 1, E1) and 5–6 August 2011 (Event 2, E2) storms. Three simulations were conducted for E1 and E2 using independent codes suitable for operational application and all hosted on the Community Coordinated Modeling Center (CCMC). The model outputs for all of the challenge events are available via http://ccmc.gsfc.nasa.gov/challenges/dBdt/. The models include: the Space Weather Modeling Framework (SWMF) adaptive grid code [*Tóth et al*., 2005, 2012; *Yu and Ridley*, 2008] which includes a global MHD model [*Powell et al*., 1999; *De Zeeuw et al*., 2000], a height-integrated ionospheric electrodynamics model [*Ridley et al*., 2001, 2002], and a ring current model (the Rice Convection Model [*De Zeeuw et al*., 2004], the Open Global Geospace Circulation Model (OGGCM) code [*Raeder et al*., 2008, 2010], and the Lyon-Fedder-Mobarry (LFM) simulation [cf. *Lyon et al*., 2004; *Merkin and Lyon*, 2010]). For E2 an additional LFM code was run that was coupled to a thermosphere-ionosphere circulation model. The specific SWPC challenge comparisons were limited to versions of these codes which could be used operationally, that is, which would be stable for general inputs and would run in real time using modest computational resources ($<$100 processors). Thus, these comparisons pertain only to the operational versions of the codes and do not reflect the capabilities or validity of more sophisticated research implementations of the simulations. For the SWMF, the version run for the challenge included a coupled inner magnetosphere module based on the Rice Convection Model [*Toffoletto et al*., 2003; *De Zeeuw et al*., 2004], but for the LFM and OGGCM simulations, a coupled inner magnetosphere module was not implemented. In addition to the simulation results, we also include comparison with the Weimer statistical model of the Birkeland currents [*Weimer*, 2005a, 2005b], hereinafter W05, because this model and a corresponding statistical model for the electric field are in general use for prediction and storm time modeling research. The model used here is from *Weimer* [2005b] and was run independently of the CCMC. To account for time delays and natural smoothing of the effects of solar wind driving in the actual response at ionospheric altitudes [cf. *Freeman et al*., 1995; *Murr and Hughes*, 2007; *Archer et al*., 2013], we smoothed the W05 model total currents using a 10 min window and delayed the W05 currents by 20 min (D. R. Weimer, personal communication, 2016).

Rather than providing metrics to assess the relative performance of the simulations, our purpose here is to identify features in the field-aligned currents most consistent or at variance with our present best measures of the behavior of the natural system to guide further development of operational versions of the models. We are not attempting to determine the extent to which the simulations correctly represent the physics of the natural system. Either simulation results could differ from the observations because some essential physics is missing, for example, the ring current, or it may reproduce the essential physics of the system at a given time but differ from the experimental data due to a parameterization that could be improved. We do not attempt to distinguish between these two causes of discrepancy. Rather, the present results are intended as a guide to identify aspects of the simulations that could be further investigated to identify the sources of any discrepancies. As with predictions of tropospheric weather, maintaining a portfolio of distinct and independent M-I simulations and models while continuing to assess the reliability of all of the predictive codes by comparison with observations is essential to determine and track our ability to predict M-I system dynamics. This motivates comparisons with the widest available set of candidate operational simulations.

Section 2 presents an overview of both storms and a comparison of the total Birkeland current, I_{Total}, from AMPERE with those from the models. Section 3 presents a detailed examination of the two-dimensional radial current density distributions, J_r, including statistical regression between the patterns for the entire storm intervals, to identify in more detail how well the models predict the system configuration at ionospheric altitudes. Section 4 summarizes the results and provides an assessment of the key findings relative to future directions.

2. Storm Events Overview

2.1. Event 1: 5 April 2010

An overview of the interplanetary magnetic field (IMF), solar wind data, integrated Birkeland currents, and *H* indices on 5 April 2010 from 0300 to 2400 UTC are shown in Figure 1. The IMF and proton solar wind data are from the Advanced Composition Explorer (ACE) spacecraft [*Smith et al.*, 1998; *McComas et al.*, 1998] at the first Lagrange point (L1). The development of magnetospheric current systems is illustrated with the total Birkeland currents derived from AMPERE (http://ampere.jhuapl.edu) together with the provisional *SYM-H* and *ASY-H* indices from the World Data Center for Geomagnetism at Kyoto University (http://wdc.kugi.kyoto-u.ac.jp/aedir/index.html). The MHD simulations were run at the CCMC using OMNI solar wind and IMF data inputs. The W05 model was run separately on a desktop computer at The Johns Hopkins University Applied Physics Laboratory also using the OMNI solar wind and IMF as input.

As in *Anderson et al.* [2014], the total Birkeland current, I_{Total}, was calculated as one half of the integral of the absolute value of the radial current density, J_r. To reduce the background noise contribution to I_{Total}, only values of $|J_r|$ greater than a typical noise level in the AMPERE inversions were included in the integral. As given also in *Anderson et al.* [2014], the net and total current over a range of colatitude θ_0 to θ_1 and a range of local times h_0 to h_1 are given by

$$I_{Net} = \frac{\pi}{12} R^2 \int_{\theta_0}^{\theta_1} \int_{h_0}^{h_1} J_r|_{>\sigma} \sin(\theta) d\theta dh \tag{1a}$$

$$I_{Total} = \frac{1}{2}\frac{\pi}{12} R^2 \int_{\theta_0}^{\theta_1} \int_{h_0}^{h_1} \mathrm{abs}(J_r)|_{>\sigma} \sin(\theta) d\theta dh \tag{1b}$$

where θ is the colatitude, R is the geocentric radius of the 780 km altitude Iridium orbits, h is local time in hours (π/12 converts from hours to radians), and "$>\sigma$" indicates that only J_r with absolute values greater than σ were included in the integral. Here θ extends from 0° (at the magnetic pole) to 50°. To determine σ, the standard deviation of J_r was evaluated from 30 quiet days, and 3 times this value is 0.16 μA/m^2 which is an estimate of the random error in J_r from AMPERE and was used for σ. To provide at least a rough distinction between dayside and nightside currents, we also compute $I_{Total,D}$ using $h_0 = 0600$ magnetic local time (MLT) and $h_1 = 1800$ MLT and $I_{Total,N}$ using $h_0 = 1800$ MLT and $h_1 = 0600$ MLT (integrating across midnight from 1800 MLT to 0600 MLT) in equation (1b). Thus, dayside and nightside total currents are defined solely by MLT without reference to ionospheric solar illumination.

To assess the random uncertainty in I_{Total}, we consider the deviation of I_{Net} from 0. Although there may be unbalanced currents [cf. *Lyatskaya et al.*, 2014], treating nonzero I_{Net} as erroneous provides an estimate of the random uncertainty in I_{Total}. Statistics of I_{Total} and I_{Net} for both events, denoted E1 and E2, are given in Table 1 together with statistics for the period before each storm, indicated as Pre-E1 and Pre-E2. The table gives the average I_{Total} and its root-mean-square (RMS), as well as the average, maximum, and minimum I_{Net} and its RMS, together with the average and RMS of $|I_{Net}|$. For the prestorm intervals the average $|I_{Net}|$ was below 0.2 MA, where MA is mega-ampere or 106 amperes, and the maximum I_{Net} was 0.7 MA. For the storm intervals the I_{Net} values were larger, with an average $|I_{Net}|$ of 0.54 MA for E1 and 0.29 MA for E2. The maximum I_{Net} was almost 1.7 MA. The $|I_{Net}|$ averages are less than about 8% of the I_{Total} average for the storms. The results from AMPERE in Figure 1 show time series $|I_{Net}|$ together with I_{Total}, $I_{Total,D}$, and $I_{Total,N}$. Although $|I_{Net}|$ is variable, it is generally small relative to I_{Total} and tends to be larger when

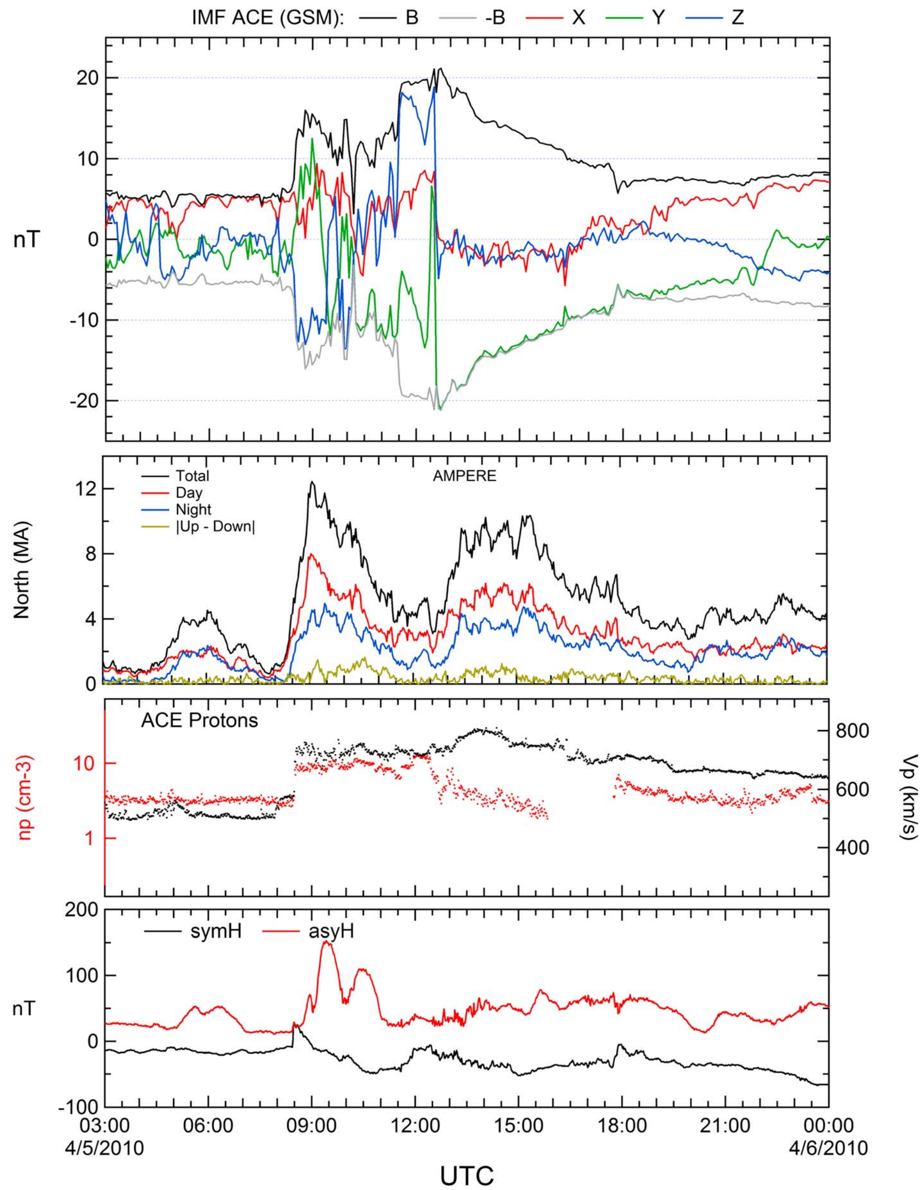

Figure 1. Overview of the 5 April 2010 storm. (first panel) The IMF at L1. Black and grey traces show B_{IMF} and $-B_{IMF}$, respectively. Red, green, and blue traces show IMF GSM Cartesian components B_X, B_Y, and B_Z. (second panel) Integrated radial Birkeland current from AMPERE with I_{Total} in black, dayside and nightside total currents in red and blue, respectively, and $|I_{Net}|$ in light brown. (third panel) The ACE solar wind proton number density (red, left axis) and speed (black, right axis) and (fourth panel) the *SYM-H* (black) and *ASY-H* (red) provisional indices. The ACE data are plotted delayed in time so that the shock signature coincides with the impulse signature in *SYM-H* near 0830 UT.

I_{Total} is also large, so a reasonable uncertainty for I_{Total} is ~8% corresponding to the approximate ratio between the average $|I_{Net}|$ and average I_{Total} for the storm periods.

The solar wind data confirm that the event started with a shock indicated by a sharp density jump from 3 to 10 protons/cm^3 and a speed increase from 580 km/s to 720 km/s at the same time as the increase in the IMF magnitude, B_{IMF}, from 6 to 13 nT. Behind the shock, the IMF turned southward with B_Z remaining slightly more negative than -10 nT until about 1000 UT. During this time, the Birkeland currents increased to over 10 MA and *ASY-H* increased dramatically to near 150 nT by 0930 UT while *SYM-H* decreased progressively to a modest minimum near -50 nT by 1000 UT. From 1000 to 1130 UT the IMF was slightly northward and dominated by a negative B_Y, but from 1130 to 1230 UT the IMF was more strongly northward and the

Table 1. Statistics of I_{Total} and I_{Net} Evaluated From AMPERE for the Two Storm Events and Time Periods Prior to Each Storm

	I_{Total}[a]		I_{Net}				$\lvert I_{Net} \rvert$	
Date/Time Range	Average	RMS	Average	Maximum	Minimum	RMS	Average	RMS
E1: 2010: 5 Apr 0815–1830	7.03	7.4	0.36	1.64	−1.48	0.63	0.54	0.63
E2: 2011: 5 Aug 1500 to 6 Aug 1700	5.62	6.84	−0.08	0.91	−1.62	0.41	0.29	0.41
Pre-E1: 2010: 2–4 Apr	2.03	2.25	0.04	0.69	−0.69	0.19	0.15	0.19
Pre-E2: 2011: 4 Aug to 5 Aug 1500	0.97	1.3	−0.08	0.39	−0.44	0.15	0.12	0.15

[a]All values in mega-amperes (MA).

Birkeland currents dropped to about 4 MA though still enhanced relative to prestorm levels. Near 1230 UT the proton density decreased and the IMF rotated to nearly purely dawnward, negative B_Y, which was sustained in direction while B_{IMF} gradually decreased, indicating the passage of the interplanetary magnetic cloud. During this time, the Birkeland currents increased again to between 8 and 10 MA and were sustained in this range. After ~1800 UT, the IMF rotated more southward as the proton speed progressively decreased, and after initially falling to below 4 MA the Birkeland currents increased slightly to between 4 and 6 MA while *SYM-H* decreased progressively reaching about −60 nT by the end of the day.

The total Birkeland current calculated from equation (1b) from AMPERE, W05, LFM, OGGCM, and SWMF for the interval are shown in Figure 2. The temporal variation of all of the models generally follows the AMPERE results with an initial surge of current from about 0900 to 1100 UT followed by an interval of lower I_{Total} and then a second period of enhanced current from about 1330 to 1530 UT. In general, the SWMF and LFM simulations give I_{Total} somewhat lower than AMPERE as does the W05 model, although the latter at times exceeds the AMPERE result. The I_{Total} from the OGGCM simulation is consistently higher than all of the other results being 5 to 10 MA higher than I_{Total} from AMPERE. Shifts in the magnitude of I_{Total} from the simulations relative to AMPERE might be partially attributed to limitations of the ionospheric conductance specifications in the simulations (all of which involve some form of semiempirical approximations).

There is a known systematic underestimation of the maximum δB and hence I_{Total} in the AMPERE results. The latitude order of the fits corresponds to ~2° latitude resolution which leads to an effective smoothing of the fitted δB relative to the input data [cf. *Waters et al.*, 2001] so that the maximum δB from the spherical harmonic fitting is systematically low relative to both the input data and other low Earth orbit (LEO) magnetometer data by roughly 30% [*Waters et al.*, 2001; *Korth et al.*, 2005; *Anderson et al.*, 2008; *Korth et al.*, 2008]. The total current is proportional to the maximum δB, so that results from the models that are higher than AMPERE up to ~30% would not indicate a real discrepancy relative to the natural system.

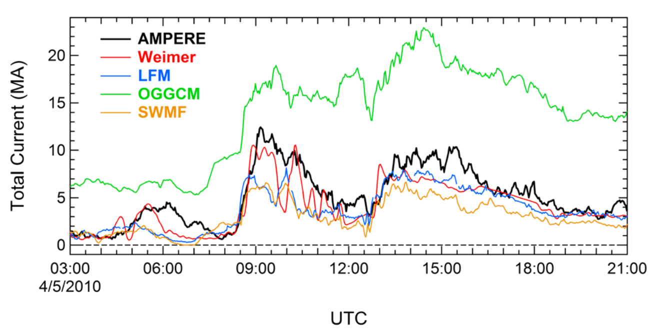

Figure 2. Time series of the total Birkeland currents for 5 April 2010 spanning the storm main phase from AMPERE, the *Weimer* [2005b] statistical model (W05), and the three MHD simulations as run for the SWPC-GEM challenge. Traces show AMPERE in black, W05 in red, Lyon-Fedder-Mobary (LFM) in blue, Open Global Geospace Circulation Model (OGGCM) in green, and Space Weather Modeling Framework (SWMF) in tan. The W05 model output results were smoothed using a 10 min average to remove unphysical instantaneous responses of the Birkeland current system to changes in the IMF and solar wind and delayed by 20 min to roughly account for time delays in the M-I system response.

Looking at some of the detailed temporal variations, the prestorm increase in I_{Total} from 0500 to 0630 UT in AMPERE, evidently driven by the preceding southward IMF interval (cf. Figure 1), is not evident in the simulation results but is present in the W05 model. From 0900 to 1030 UT the W05 model shows a pronounced, relatively short lived, decrease in I_{Total} centered near 1000 UT to between 4 and 5 MA, which is not present in the AMPERE I_{Total}. The W05 model shows more variability in I_{Total} than

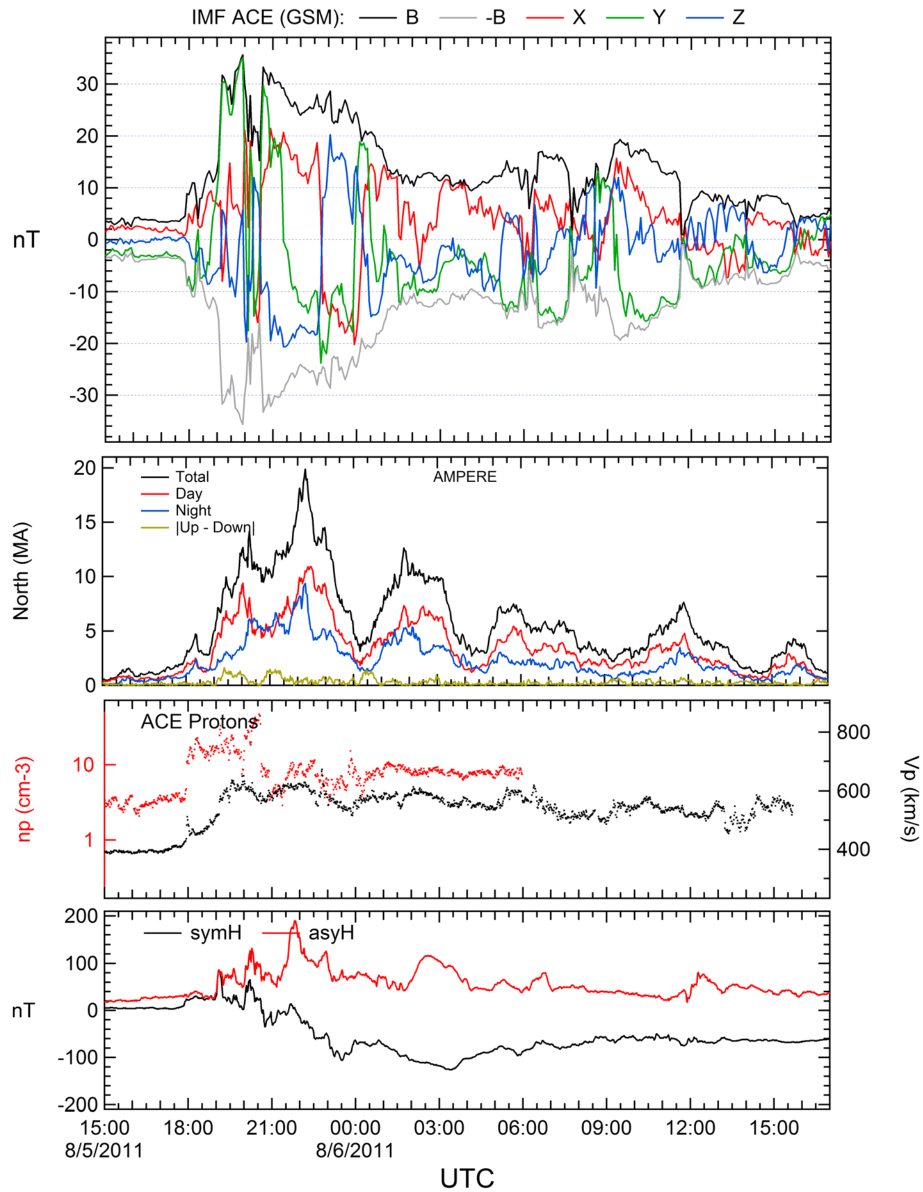

Figure 3. Overview of the 5–6 August 2011 storm in the same format as in Figure 1. The ACE data are plotted delayed so that the solar wind density jump coincides with the impulse signature in *SYM-H* near 1800 UTC.

either AMPERE or the simulations, possibly implying that the M-I system moderates its response to variations in the solar wind/IMF driver [*Freeman et al.*, 1995; *Murr and Hughes*, 2007; *Archer et al.*, 2013], and this natural "low-pass filtering" is not yet included in the empirical model other than via the averaging discussed above.

2.2. Event 2: 5–6 August 2011

The overview for the second event is shown in Figure 3. For this event, onset near 1800 UT was marked by an increase in proton density without a corresponding sustained increase in speed, and an increase in B_{IMF} from 4 nT to near 10 nT. Nonetheless, the increase in solar wind ram pressure is indicated by an increase in *SYM-H* to about +20 nT, and the ACE data were time shifted to match the density increase to this *SYM-H* signature. The Birkeland currents increased slightly from ~2 MA to near 4 MA. Near 1900 UT, there was a large increase in B_{IMF} from 10 nT to near 30 nT, dominated by a positive B_Y, and an increase in the proton speed from ~520 km/s to ~580 km/s. This led to a substantial growth of the Birkeland currents, almost entirely on the dayside, to ~7 MA. The first interval of sustained southward IMF started shortly before 2100 UT and continued until 2300

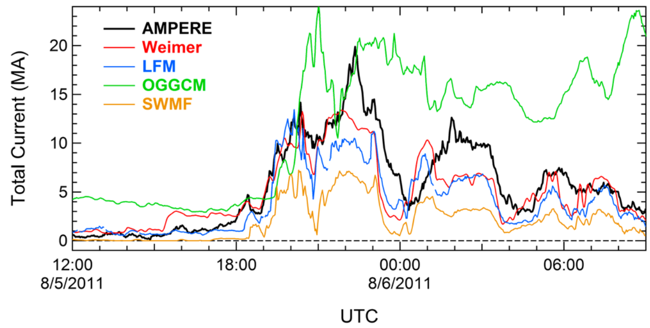

Figure 4. Time series of the total Birkeland currents for 5–6 August 2011 spanning the storm main phase from AMPERE, the W05 model, LFM, OGGCM, and SWMF MHD simulations as run for the SWPC-GEM challenge. Format is the same as in Figure 2.

UT and corresponds to a progressive decrease in *SYM-H* to −60 nT and sustained Birkeland currents over 12 MA. At the end of this interval the Birkeland currents increased sharply and briefly to 20 MA due primarily to nightside currents. Thereafter the IMF turned northward, and the Birkeland currents decreased progressively to less than 5 MA. At 0030 UT on 6 August, the IMF turned southward again, and by 0130 UT the Birkeland currents had grown to 9 MA and remained elevated until 0310 UT when they began to decrease after the IMF turned away from southward, dominated by a positive B_X component. The minimum *SYM-H* of −120 nT occurred at 0310 UT. Thereafter there were two periods of increased Birkeland currents but they remained below 8 MA while *SYM-H* gradually increased during early storm recovery. As for E1, $|I_{Net}|$ remained small relative to I_{Total}.

The temporal behavior for I_{Total} from AMPERE and the models for this event are shown in Figure 4. All of the models show a small increase in I_{Total} near or shortly after 1800 UT, and I_{Total} increases markedly starting near 1900 UT, consistent with the AMPERE result. The W05 and LFM results increase nearly in concert and to the same current as AMPERE, ~10 MA, to 2000 UT, whereas the SWMF current increases to ~5 MA and in OGGCM to ~8 MA by 2000 UT. The OGGCM current continues to increase to over 20 MA by 2030 UT and reaches 24 MA by 2100 UT after which it drops to ~10 MA, whereas the AMPERE current is fairly level between 10 and 13 MA. At the time of the ~1 h "spike" in the OGGCM current, the other models exhibit a brief decrease in I_{Total} to ~7 MA in W05, ~5 MA in LFM, and under 2 MA in SWMF. The surge in I_{Total} from 2130 to 2200 UT to nearly 20 MA in AMPERE is matched only in the OGGCM result, while none of the other models show this feature. The increase in the AMPERE current is due to a 5 MA surge in the nightside current together with a slower increase in the dayside current (cf. Figure 3). The burst in the nightside current is due to a sudden onset in the premidnight sector (see section 3.2 below) and is attributed to magnetotail dynamics not represented in the LFM or SWMF simulations or W05. As discussed in section 3.2, the OGGCM J_r distribution does not match the nightside onset observed in AMPERE even though the AMPERE and OGGCM I_{Total} increases track each other. Shortly after 2200 UT and until shortly after 0000 UT on 6 August, the AMPERE currents dropped progressively to under 5 MA and all of the models except OGGCM exhibit a similar significant fall in I_{Total}, albeit with different timing, preceding the I_{Total} decrease in AMPERE by 30 to 60 min. The OGGCM currents fall only slightly from 20 MA to ~16 MA, and from this point onward the I_{Total} from OGGCM remains above 12 MA and even increases back to over 20 MA near the end of the interval. This is markedly different from the behavior in AMPERE, which exhibits two surges in I_{Total}: the first to ~10 MA from ~0100 to 0300 UT associated with the second sustained southward IMF interval noted above and the second to ~7 MA near 0500 UT. The SWMF, LFM, and W05 results all have a short-lived increase in I_{Total} peaking near 0100 UT on 6 August which is not present in AMPERE. This coincides with the similar short southward turning of the IMF at L1 so that the three models evidently reflect this behavior at L1 which the natural system did not exhibit, possibly owing to uncertainties in extrapolating the L1 observations of upstream conditions to Earth [cf. *Merkin et al.*, 2013]. Otherwise, the other models have features broadly similar to the two broad, >3 h long surges in AMPERE I_{Total}, although the levels and timing differ somewhat with SWMF being consistently low. As in Event 1, the LFM and W05 currents seem to be generally the most similar to AMPERE.

2.3. Statistical Comparisons of Total Current

To quantify the comparisons of the total current, we performed linear regressions between the model time series in Figures 2 and 4 and the AMPERE I_{Total} results for the time spans shown in the plots. We write the linear fits as

Table 2. Summary of Results for Linear Regression and Ratios Between Model and AMPERE Total Birkeland Currents

Event	Model	a	σ_a	b	σ_b	C_L	Ratio	σ_{Ratio}
4–5 Apr 2010	W05	0.989	0.146	0.620	0.025	0.73	0.94	0.62
4–5 Apr 2010	LFM	0.616	0.105	0.617	0.018	0.83	0.83	0.40
4–5 Apr 2010	SWMF	0.378	0.078	0.508	0.013	0.86	0.68	0.46
4–5 Apr 2010	OGGCM	6.615	0.262	1.394	0.044	0.81	3.47	2.03
5–6 Aug 2011	W05	1.704	0.145	0.584	0.02	0.76	1.36	1.02
5–6 Aug 2011	LFM	0.444	0.094	0.643	0.013	0.89	0.92	0.62
5–6 Aug 2011	SWMF	−0.24	0.058	0.402	0.008	0.90	0.28	0.19
5–6 Aug 2011	OGGCM	6.48	0.332	0.915	0.046	0.62	3.52	3.11

$$I_{\mathrm{Total,Model}} = a + bI_{\mathrm{Total,AMPERE}} \tag{2}$$

where $I_{\mathrm{Total,Model}}$ and $I_{\mathrm{Total,AMPERE}}$ are the model and AMPERE total currents, respectively. The results are summarized in Table 2 where σ_a and σ_b are the 1 sigma standard errors in a and b, and C_L is the linear regression coefficient. In addition, we computed the average of the ratio $I_{\mathrm{Total,Model}}/I_{\mathrm{Total,AMPERE}}$, denoted simply as "Ratio," and its standard deviation, σ_{Ratio}.

The intercepts (values for "a") in the LFM and SWMF are both less than 1 MA, whereas for W05 they are near 1 MA or a bit higher, and for the OGGCM model the intercept is slightly higher than 6 MA. This suggests that much of the apparent excess in OGGCM total current is a baseline current, reflecting the tendency of the OGGCM current to be relatively high, above 5 MA, prior to the storm intervals, even when the AMPERE current is low, e.g., from 0300 to 0500 UT on 5 April 2010 and 1200 to 1700 UT on 5 August 2011. The linear fit slopes on the other hand are closest to unity for the OGGCM simulation and are significantly below 1 for the other models with SWMF giving the lowest average b reflecting the consistently low results for the SWMF I_{Total} relative to AMPERE. Of the simple metrics used here, the linear regression coefficient gives perhaps the best measure of the predictive ability of the models relative to AMPERE. The C_L values for all of the models are relatively high, above 0.7, with the SWMF slightly higher C_L values than LFM, although they are so close as to be essentially indistinguishable.

The ratio comparisons reflect that OGGCM is consistently higher than AMPERE by a factor of 2 to 3 whereas W05 is fairly close in its ratio to AMPERE, consistent with the results of the linear fit slope. In summary, all of the models show the general behavior of I_{Total} reflected in the AMPERE results but none of them clearly stands out as superior even though there are some consistent trends, such as the higher and lower currents from OGGCM and SWMF, respectively.

3. Birkeland Current Distributions

The comparisons of I_{Total} do not distinguish the locations or configuration of the Birkeland currents. We therefore compare the two-dimensional distributions of the radial current density, J_r, for AMPERE and the models. We prepared maps of J_r at 2 min intervals for the entire time spans shown in Figures 2 and 4. The AMPERE J_r distributions were determined every 2 min using 10 min spans of data [cf. *Clausen et al.*, 2012; *Anderson et al.*, 2014]. Since the AMPERE intervals start on even minutes, e.g., 0300, 0302, and 0304 UT, the model J_r were retrieved on the corresponding centered odd minutes, e.g., 0305, 0307, and 0309 UT. That is, the comparison for 0305 UT used the models evaluated at that time and AMPERE data for the 0300 to 0310 UT interval.

For the models and simulations, the J_r distributions at each time were registered on the same MLT-magnetic latitude (MLAT) grid in the Northern Hemisphere. We used the Northern Hemisphere for two reasons. First and most importantly, the ground magnetometers used to compare the model results were from the Northern Hemisphere [e.g., *Pulkkinen et al.*, 2013]. Second, the AMPERE results tend to be more reliable in the north because the orbit crossing point of the Iridium satellite constellation tends to lie near the southern auroral zone but poleward of the auroral zone in the north. In the present generation of data processing and inversions, the J_r inversions from AMPERE yield spurious filamentary currents near the orbit crossing location and this is minimized in Northern Hemisphere inversions.

In the comparisons with the AMPERE J_r distributions, it is important to bear the limitations of the AMPERE inversions in mind. The inversions used here have a latitude order of 60 spanning from the pole to 60° colatitude, which corresponds to a latitude resolution of the inversions of ~2° [cf. *Waters et al.*, 2001; *Anderson* *et al*., 2014]. This relatively coarse latitude resolution implies that the natural current systems are at least as narrow as the AMPERE J_r distributions. This also implies that the J_r from AMPERE underestimate the true current densities, and the degree of underestimation is roughly proportional to the ratio of the latitude resolution of the AMPERE fit and the actual latitude width of the currents. Although the large-scale currents occur with latitude scales of a few degrees, the AMPERE J_r underestimation is not always large, but large gradients in the large-scale currents, hundreds of nanotesla, do occur in times as short as 1 s [e.g., *Anderson et al*., 1993; *Ohtani et al*., 2012; *He et al*., 2012] which corresponds to roughly 0.1 km, so that the AMPERE J_r could be as much as a factor of 10 or 20 low on occasion. Although it is not possible to determine how much the AMPERE J_r underrepresent the actual J_r for each location of every 10 min interval, we can be confident that the real currents are at least as narrow in latitude as the AMPERE products and that the actual current densities are at least as high as the AMPERE results. One can also be confident that the locations of the AMPERE currents reflect the natural system within the colatitude range (60° colatitude), latitude resolution (2°), and local time resolution (2 h) of the input data and the inversions.

3.1. Event 1: 5 April 2010: J_r Patterns and Correlation

Three times were selected from the 5 April 2010 storm to illustrate the types of comparisons between J_r from AMPERE and the models, and they are shown in Figures 5–7. Figures 5a, 6a, and 7a show the J_r distributions with upward current in red and downward current in blue for AMPERE on the upper left, W05 in the top center, and LFM, OGGCM, and SWMF in the lower portion from left to right. Figures 5b, 6b, and 7b show scatterplots of J_r from W05, LFM, OGGCM, and SWMF versus AMPERE J_r together with the linear fit and regression coefficient in red for each time interval. Figures in this format were created for every odd minute for the time spans of Figures 2 and 4.

The first time, 0907 UT on 5 April 2010 shown in Figure 5, corresponds to the first local maximum in AMPERE I_{Total} after storm onset (cf. Figures 1 and 3). Focusing initially on the latitude ranges with significant J_r in Figure 5a, we first note that the AMPERE currents span from 65° to 75° MLAT near noon; elsewhere they are present from 50° to 60° MLAT. The Region 1/Region 2 currents in the W05 model are broader, extending from 40° MLAT to slightly poleward of 70° MLAT. (We use the Region 0, Region 1, and Region 2 terminology for the currents only in reference to their average location rather than attempting to assign currents by these terms since the AMPERE distributions are not always well ordered by these systems, and the different regions appear to gradually shift and merge as the IMF clock angle rotates [cf. *Anderson et al*., 2008; *Korth et al*., 2010]). By contrast, the LFM currents, dominated by the Region 1 sense system, span from 70° to 80° MLAT while the SWMF Region 1 sense currents are slightly more equatorward. The Region 2 sense currents in SWMF extend to ~60° MLAT. Currents in the OGGCM simulation are present over latitudes very similar to AMPERE, although they occur about 5° farther equatorward near noon than they do in AMPERE. That the SWMF results obtain an evident Region 2 current is expected since this is the only code in which the operational test version was coupled to a ring current/inner magnetosphere model. Thus, the apparent low intensity of Region 2 currents in the LFM code is to be expected, but the Region 2 sense currents in the OGGCM results are somewhat surprising. We note, however, that the lower latitude currents in the OGGCM results are neither as consistently present nor as uniformly structured in longitude as those in the SWMF or in AMPERE, so that in this code as well, a consistent Region 2 sense system is not as evident as it is in the SWMF.

The current intensities in W05, LFM, and SWMF are all substantially lower than those in AMPERE, while those in the OGGCM are higher. This relative difference in J_r magnitudes is reflected in the scatterplots by the range of J_r from each model. This ordering in relative current intensities with SWMF tending to be the lowest, followed by W05, then LFM, then AMPERE, and OGGCM being strongest, holds in almost all frames examined for these two storms.

Turning to the J_r patterns, although the IMF was southward, there was also a significant positive B_Y component (cf. Figure 1). The AMPERE currents show a region of downward current that extends from the nominal Region 1 dawn currents, across noon (sometimes termed Region 0), to the equatorward downward currents in the afternoon and evening (Region 2). Upward currents in AMPERE are rotated clockwise relative to an average southward IMF pattern and occur in the predawn morning equatorward of the upward currents and poleward of the downward currents in the afternoon with some weaker currents slightly toward midnight from dusk. This skewed distribution is typical of southward IMF with a strong

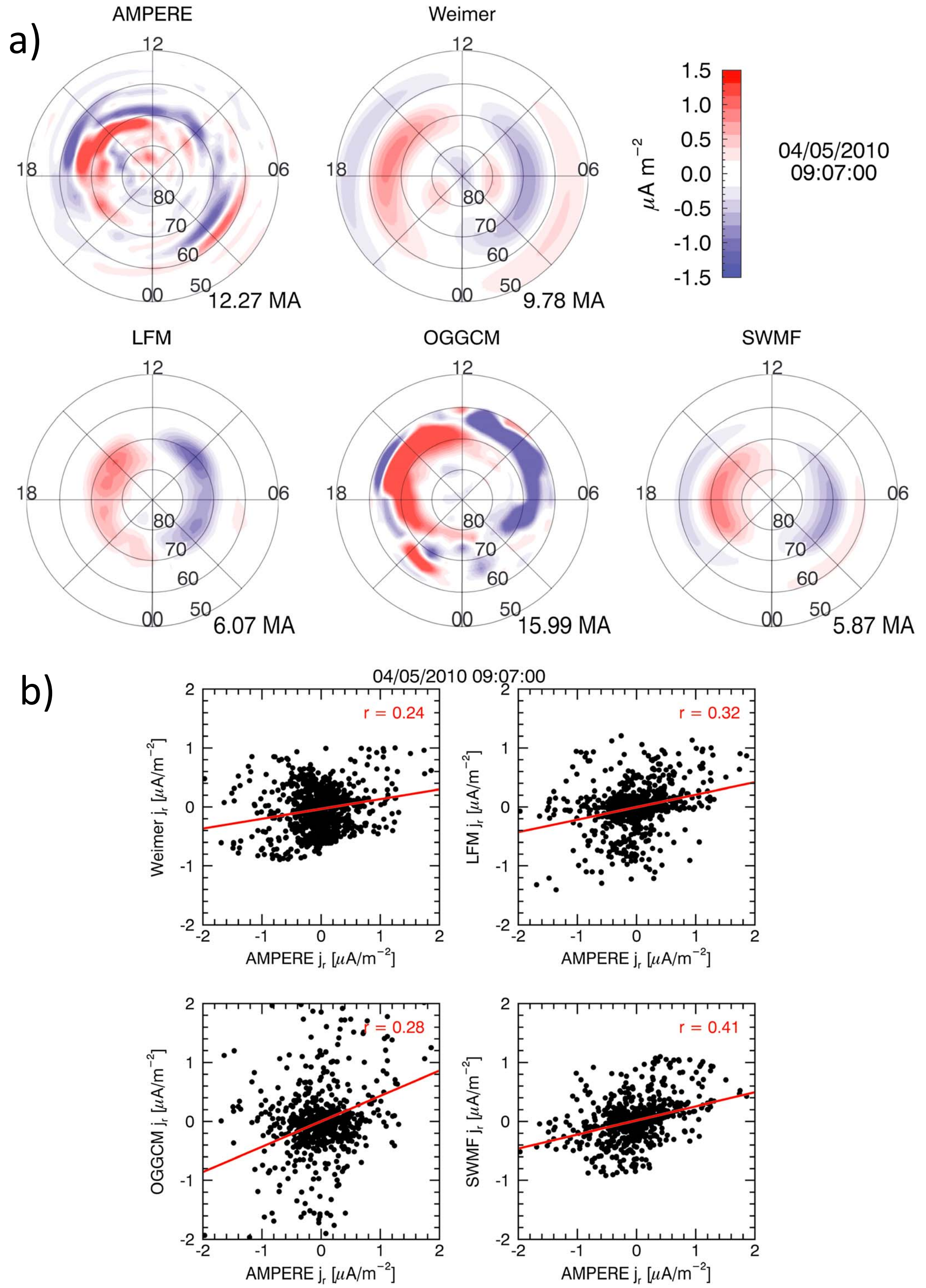

Figure 5. Comparisons of radial current density, J_r, for 0907 UTC on 5 April 2010 near storm onset. (a) Distributions of J_r versus magnetic latitude and local time from AMPERE, W05, LFM, OGGCM, and LFM. AMPERE results are for the 10 min interval centered on 0907 UTC, that is, 0902–0912 UTC. Upward (downward) current is in red (blue) as shown by the color bar, and the I_{Total} for each distribution is given with each distribution. Values above 1.5 μA/m^2 or below −1.5 μA/m^2 are saturated. (b) Scatterplots of J_r from each model versus AMPERE J_r together with the linear fit between them, and the linear regression coefficient, r, is given in each scatterplot.

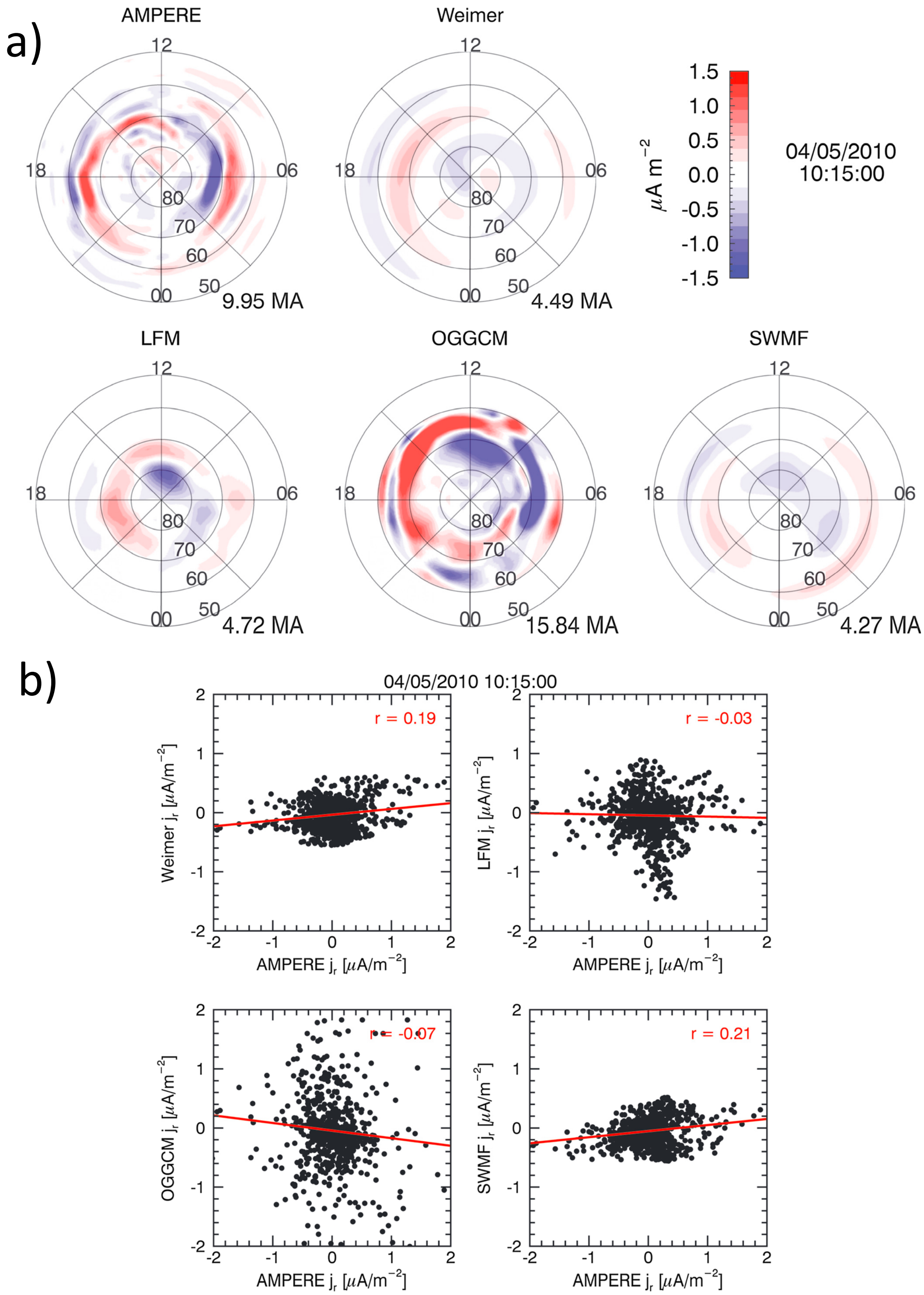

Figure 6. Comparisons of radial current density, J_r, for 1015 UTC on 5 April 2010 during storm main phase. AMPERE results are for the 10 min interval, 1010–1020 UTC. Format is the same as in Figure 5.

positive B_Y [cf. *Anderson et al.*, 2008; *Korth et al.*, 2010]; although there may be hints of a dawn-dusk asymmetry in the W05, LFM, and SWMF results, none of these models yield the degree of asymmetry observed. The J_r distributions for these models are generally substantially different than J_r from AMPERE. The OGGCM simulation yields the strongest asymmetry, but it also departs substantially from the AMPERE pattern.

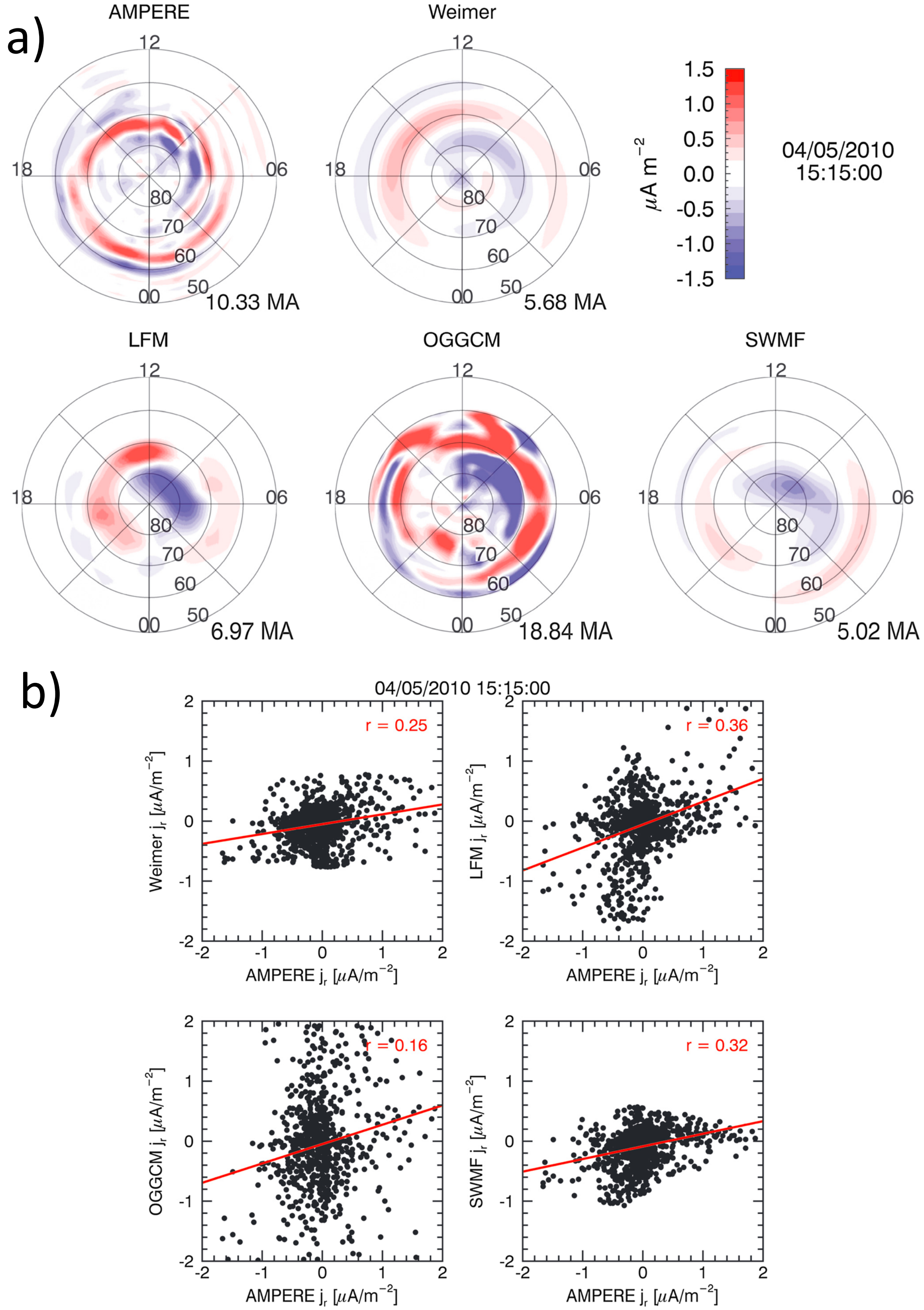

Figure 7. Comparisons of radial current density, J_r, for 1515 UTC on 5 April 2010 late in the storm main phase. AMPERE results are for the 10 min interval, 1510–1520 UTC. Format is the same as in Figure 5.

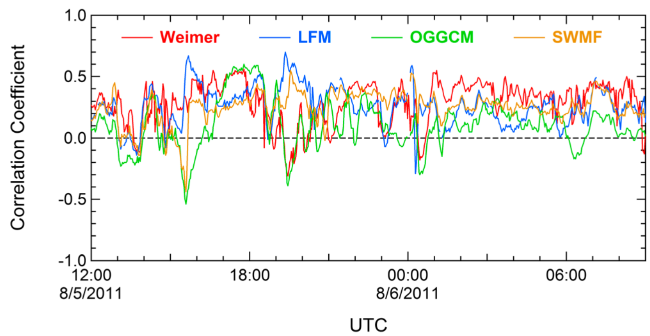

Figure 8. Time series of linear correlation coefficients between model/simulated and AMPERE J_r distributions for the same time interval as in Figure 2, spanning the storm main phase on 5 April 2010. Colors are the same as in Figure 2 with W05 in red, LFM in blue, OGGCM in green, and SWMF in tan.

The dissimilarities in the J_r distributions are reflected in the consistently low correlations in the scatterplots and linear fits. There are substantial areas where the J_r are positive in AMPERE but negative in a model or vice versa, reflecting relative displacement of the J_r distributions in either latitude or longitude or both. The regression coefficients are correspondingly low ranging from 0.24 to 0.41. This comparison is particularly sensitive to displacement in the currents, and a negative regression coefficient could result even if the patterns in J_r are very similar but are substantially displaced in latitude. A more sophisticated comparison based on similarity in the shape of the J_r patterns and degree of overlap could be useful in future analyses and inform other quantitative metrics [e.g., *Korth et al.*, 2010; *Kleiber et al.*, 2016; *Wiltberger et al.*, 2016].

The second set of frames is from 1015 UT, 1010–1020 in AMPERE, and is shown in Figure 6. This corresponds to near the end of the first interval of enhanced I_{Total} in Figure 2 and near the time of the northward IMF rotation in Figure 1. The AMPERE currents remain elevated near 10 MA, while the W05, LFM, and SWMF I_{Total} values have fallen sharply to under 5 MA. The distributions illustrated the marked differences between the J_r distributions observed via AMPERE and the modeled distributions. The AMPERE distribution exhibits a fairly strong system very similar to the statistical Region 1/Region 2 system, and, whereas the W05 pattern retains a relatively weak Region 1/Region 2 pattern, the polar cap currents of the polarity of northward B_Z currents have equally intense J_r. The SWMF pattern is similar to the W05 result, and the LFM currents are dominated by high-latitude currents not evident in the AMPERE result. The OGGCM pattern is most similar to that from AMPERE, although the polarity ordering at noon appears to be reversed with the equatorward strong current being upward in OGGCM but downward in AMPERE. Interestingly, both the SWMF and LFM codes yield R2 sense currents suggesting that this system is not entirely absent without the inner magnetosphere module. The scatterplots and linear correlation results reflect the low correspondence evident in the patterns, and the regression coefficients are quite low ranging from −0.07 to 0.21. Even though the OGGCM pattern is the most similar to AMPERE, the linear regression coefficient is actually negative, reflecting the latitude displacement of the two results on the dayside where the J_r magnitudes are high.

The third frame shown in Figure 7 is for 1515 UT, 1510–1520 UT in AMPERE, corresponding to the period of stably directed IMF predominated by a negative B_Y and at a time of enhanced nightside I_{Total} in AMPERE (cf. Figure 1). The AMPERE currents exhibit an upward current region that extends from poleward at dusk, across noon, to the equatorward upward currents at dawn, characteristic of negative IMF B_Y, and a downward/upward pair of currents extending from just predawn to dusk, which is the current system responsible for the enhancement in the nightside I_{Total} at this time (Figure 1). All of the models display a dayside set of currents with a poleward downward current across noon broadly similar to the highest latitude downward current on the dayside in AMPERE. The W05, OGGCM, and LFM results also exhibit an upward current across noon that is contiguous with the dusk “Region 1” and dawn “Region 2” currents. This dayside upward current does not appear in the SWMF result. All of the models have Region 2 currents across dusk and across dawn that are also evident in AMPERE. Only the OGGCM result has currents that resemble the pair of currents that cross the entire nightside in AMPERE.

This interval was chosen to illustrate another common feature in the comparisons. Nightside current pairs are often observed in AMPERE in association with nightside enhancements in I_{Total}, related to substorm-like behavior during storms [*Anderson et al.*, 2014; *Coxon et al.*, 2014; *Lyons et al.*, 2016], and are generally not evident in the W05, SWMF, or LFM models. The scatterplots of J_r and linear regressions show greater correlation at this time, ranging from 0.16 to 0.36. Typically, the models do not capture these nightside onset current systems.

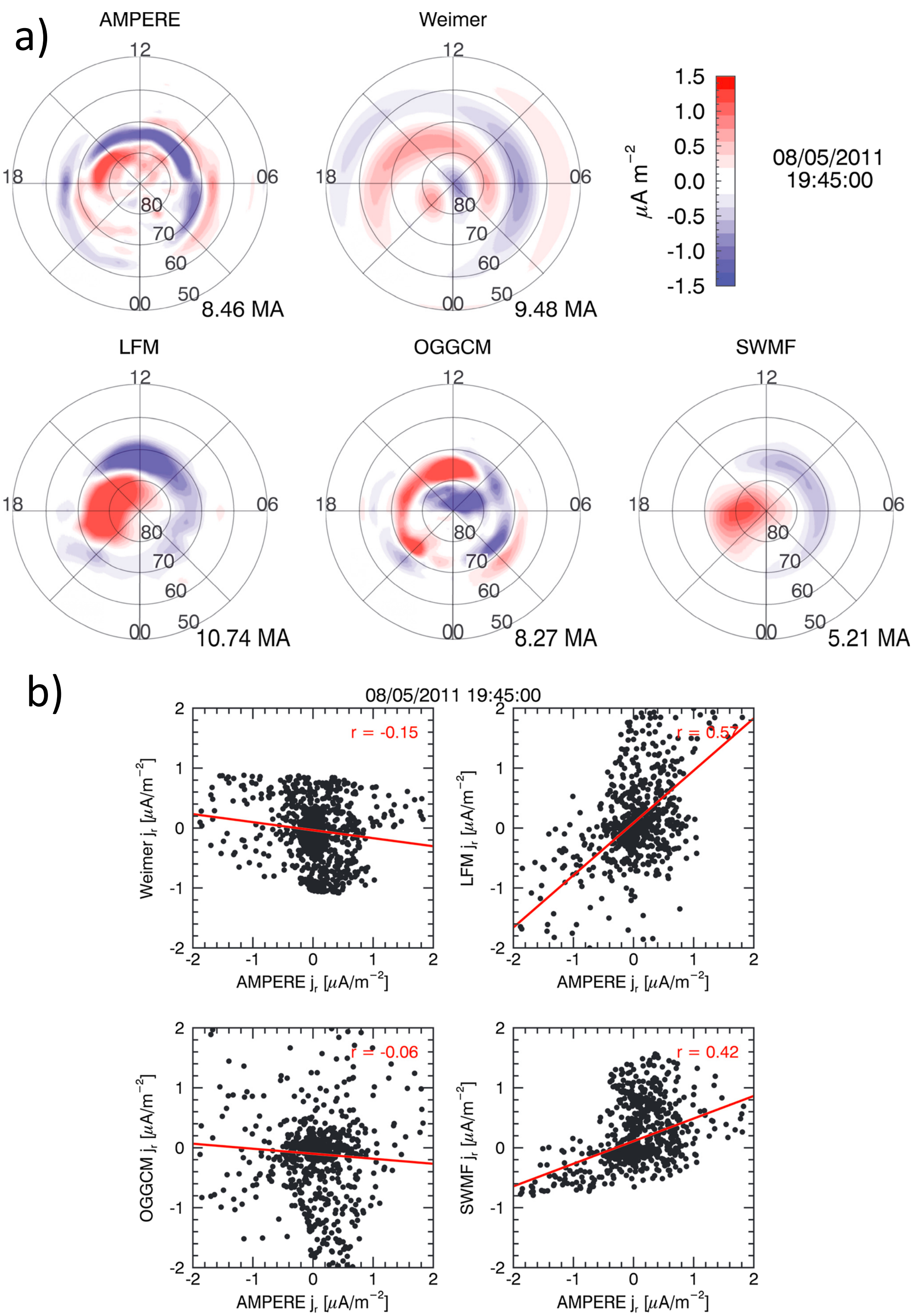

Figure 9. Comparisons of radial current density, J_r, for 1945 UTC on 5 August 2011 near storm onset. AMPERE results are for the 10 min interval, 1940–1950 UTC. Format is the same as in Figure 5.

To summarize the J_r comparisons for E1, the time series of the linear regression coefficients are plotted in Figure 8 for the time span shown in Figure 2. No model has a uniformly high correlation with the AMPERE J_r, and all of the models vary but range between 0.0 and 0.5. The OGGCM regression coefficient is usually lower than the others possibly reflecting the fact that the J_r in OGGCM are strong and often displaced relative to

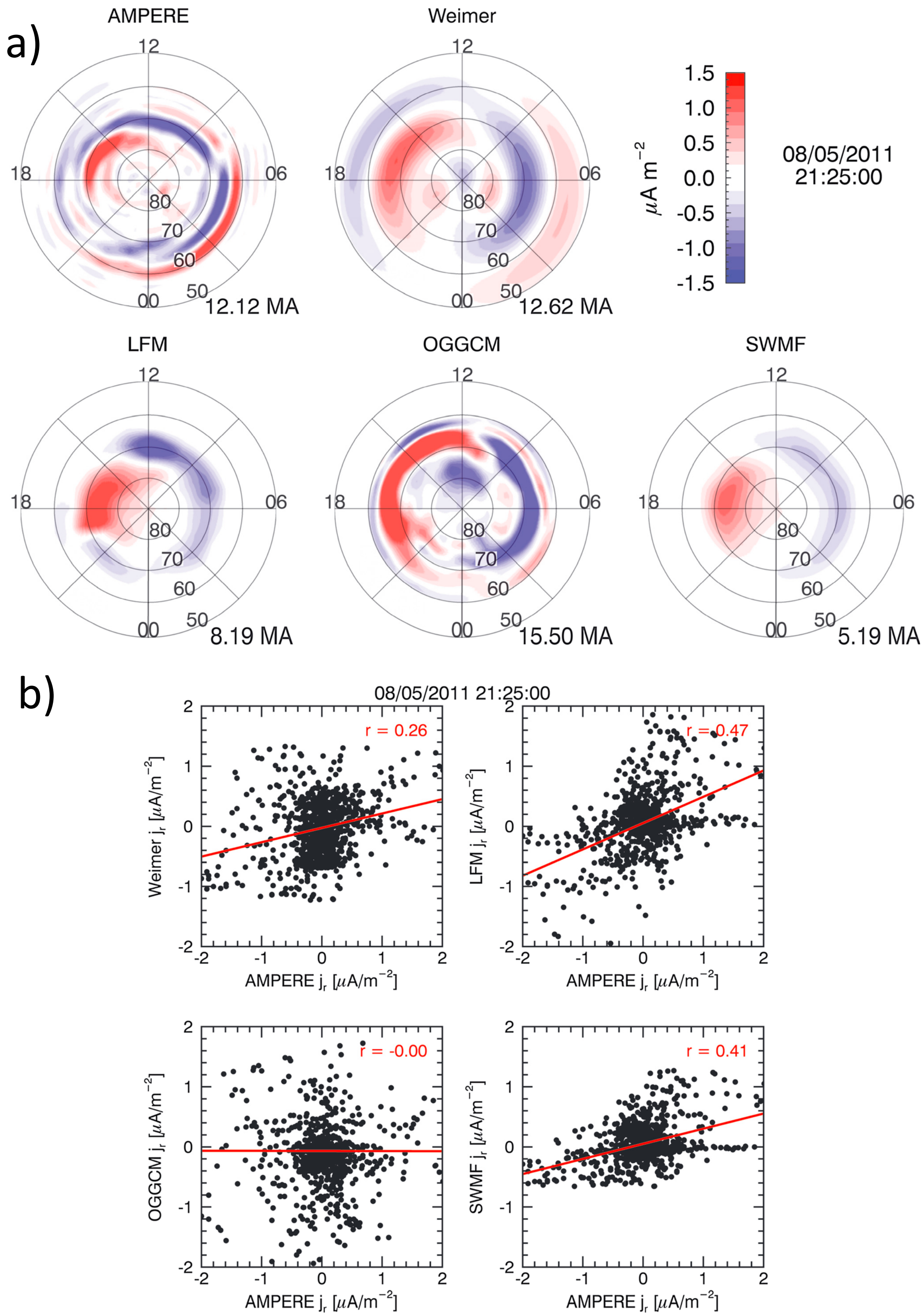

Figure 10. Comparisons of radial current density, J_r, for 2125 UTC on 5 August 2011 during storm main phase. AMPERE results are for the 10 min interval, 2120–2130 UTC. Format is the same as in Figure 5.

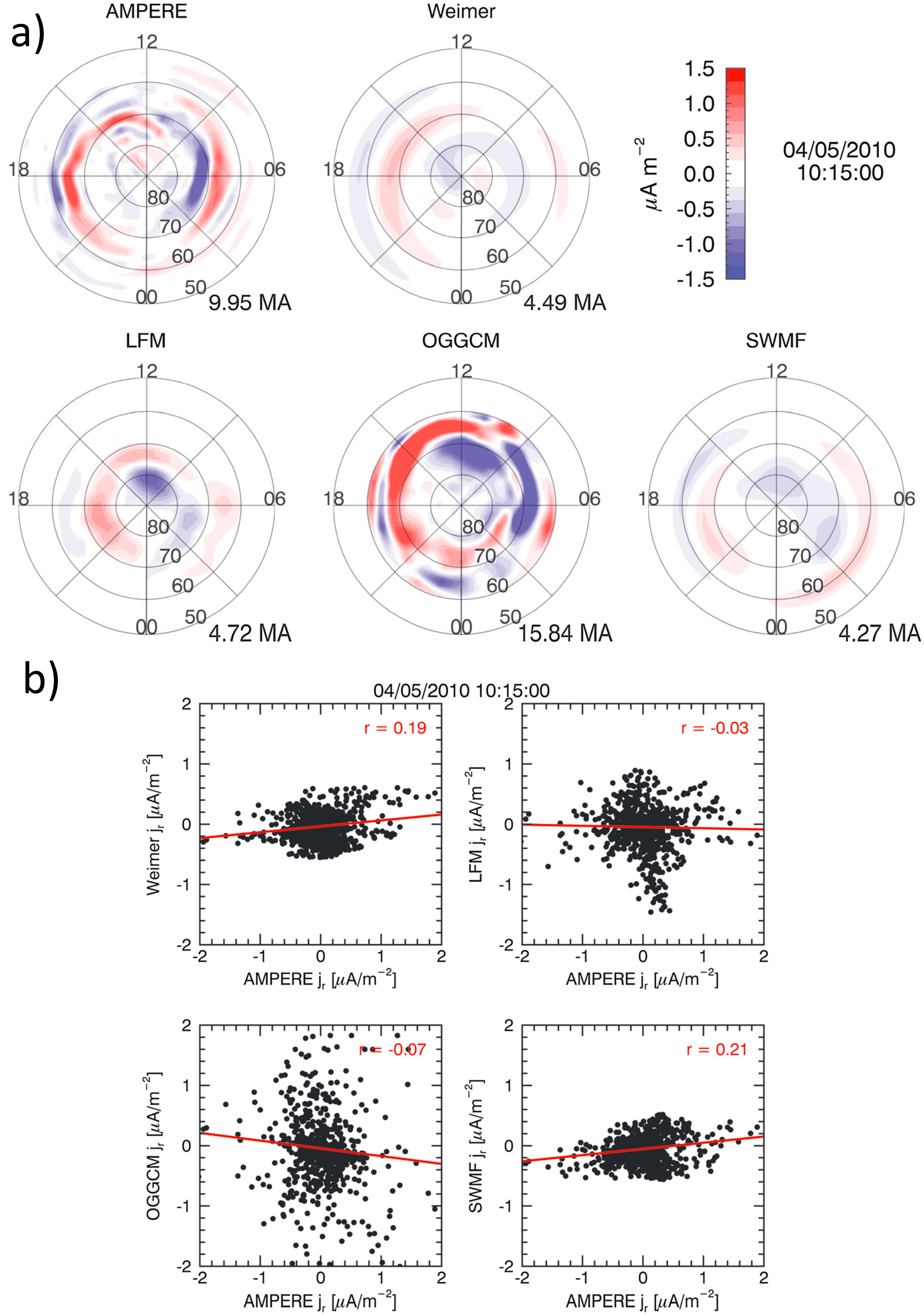

Figure 11. Comparisons of radial current density, J_r, for 2215 UTC on 5 August 2011 during storm main phase at a time on a sharp onset of nightside currents. AMPERE results are for the 10 min interval, 2210–2220 UTC. Format is the same as in Figure 5.

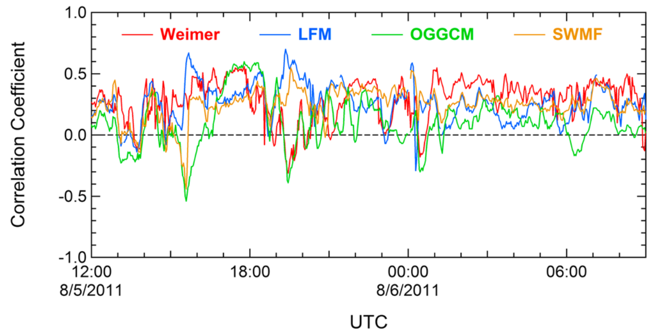

Figure 12. Time series of linear correlation coefficients between model/simulated and AMPERE J_r distributions for the same time interval as in Figure 2, spanning the storm main phase on 5 and 6 August 2011. Format is the same as in Figure 8.

AMPERE particularly on the dayside. For this event, the SWMF results yielded a consistent Region 2 sense current system which, although often present in the other simulations, was less consistently evident or as strong as the Region 1 currents.

3.2. Event 2: 5–6 August 2011: J_r Patterns and Correlation

Similar comparisons for three specific times during E2 are shown in Figures 9–11. The first time, 1945 UT, 1940–1950 UT in AMPERE, shown in Figure 9, illustrates the currents near the end of the IMF B_Y positive interval at the start of this storm. The W05, LFM, and SWMF J_r distributions all exhibit a downward current extending from a dawn Region 2 sense current across noon with an upward current more poleward of this at noon. Curiously, the OGGCM dayside currents show the opposite polarity in these high-latitude dayside currents. The morning Region 2 current is most evident in the OGGCM result although only at night. A Region 2 sense current, downward, is present in both the OGGCM and LFM codes but is not evident in the SWMF result. The W05 currents for this time extend about 10° farther equatorward than the AMPERE results. The LFM and SWMF do not yield the upward/downward current pairs on the nightside in the evening and morning, though the OGGCM result does.

The scatterplots for this time reflect the large latitude displacement between AMPERE and W05 and the reversed dayside current polarities with OGGCM and AMPERE with negative correlation coefficients for both models. The LFM and SWMF results are positively correlated with AMPERE giving fairly high coefficients of 0.51 and 0.42, respectively, owing to the strong high-latitude dayside currents.

The second time frame shown in Figure 10 is for 2125 UT, 2120–2130 UT in AMPERE, shortly before the B_Y reversal from positive to negative during southward IMF (cf. Figure 3). The AMPERE currents exhibit a similar downward current from dusk Region 2, across noon, to dawn Region 1 as for the previous interval and the interval from E1 in Figure 5. The W05, LFM, and SWMF results exhibit a similar upward current pattern. The W05 currents extend ~10° farther equatorward than AMPERE, and the currents in SWMF and LFM are broader in latitude, as for the other cases. Both LFM and SWMF have a strong upward current in the afternoon corresponding to the most poleward upward current in the afternoon in the AMPERE J_r pattern. The OGGCM result has an additional high-latitude downward current centered at noon which may be due to the B_Y reversal that preceded this frame. Neither the LFM nor SWMF exhibit the strong equatorward Region 2 sense currents present in AMPERE, which are strongest in the W05 result and present somewhat in the OGGCM result. None of the models return the intense upward current that extends from premidnight to dawn in the AMPERE results. The scatterplots for this time reflect the broad correspondence in the dayside currents, yielding positive correlations with W05, LFM, and SWMF. The polarity of the dayside currents and latitude displacements lead to the low correlation with OGGCM.

Table 3. Average of Linear Regression Results Between Radial Current Density Distributions of Models and AMPERE Birkeland Radial Current Density

		Coefficient		Slope	
Event	Model	$\langle C_L \rangle$	σ_{CL}	a	σ_a
4–5 Apr 2010	W05	0.20	0.14	0.14	0.10
4–5 Apr 2010	LFM	0.24	0.14	0.28	0.17
4–5 Apr 2010	SWMF	0.28	0.08	0.19	0.07
4–5 Apr 2010	OGGCM	0.11	0.10	0.26	0.25
5–6 Aug 2011	W05	0.29	0.17	0.28	0.20
5–6 Aug 2011	LFM	0.26	0.16	0.29	0.20
5–6 Aug 2011	SWMF	0.25	0.13	0.14	0.09
5–6 Aug 2011	OGGCM	0.10	0.20	0.20	0.42

The final frame is for 2215 UT, 2210–2220 UT in AMPERE and is shown in Figure 11. This corresponds to the early portion of the negative B_Y interval after the B_Y reversal. As with the 1515 UT frame from E1, in the AMPERE J_r, the Region 1 sense dusk upward current appears to extend across noon to the Region 2 sense dawn current. A similar upward current extension across noon from dusk is present in the W05, LFM, and SWMF results, although OGGCM seems to have the opposite signature, perhaps retained from the prior positive B_Y interval. The dawn upward and dusk downward Region 2 currents are now clearest in the LFM result. This interval was selected primarily because of the additional downward/upward currents in the dusk to midnight sector in AMPERE which is present in none of the models, illustrating the nightside dynamics in Birkeland currents that are not evident in the models even though this type of current system is not unusual in AMPERE storm time currents [cf. *Lyons et al*., 2016]. The scatterplots for this frame show positive correlations with all of the model results, including OGGCM indicating that the strong dusk and dawn currents are dominating the regression with AMPERE for this model at this time.

The time series of the AMPERE model regression coefficients for E2 are shown in Figure 12, and as with E1, the correlations are modestly positive, but for this storm there are several intervals of clearly negative correlation which are with SWMF and OGGCM near 1530 UT, with OGGCM and W05 near 1915 UT, and with OGGCM and W05 near 0015 UT on 6 August. In general, the correlation between J_r from AMPERE and the models is fairly low, as for E1, reflecting the considerable differences in the J_r distributions during the storm. For this case, the Region 2 currents when present in the simulation results were more evident in the LFM and OGGCM results rather than the SWMF result, which is somewhat surprising given that only the SWMF included a coupled inner magnetosphere module.

3.3. Statistical Assessment

To summarize the results for the J_r comparisons, we evaluate the average linear correlation coefficients, C_L, as well as the average linear fit slopes, a, relative to AMPERE for both events. The results are given in Table 3 together with the standard deviations of C_L and a, denoted σ_{CL} and σ_a, respectively. The average C_L are low, ranging from 0.1 to 0.29 with σ_{CL} that are only slightly lower reflecting the variation in the generally weak correlations. The average slopes are also low, ranging from 0.14 to 0.29, also with substantial scatter indicated by the comparable values of σ_a. These averages indicate that although the I_{Total} are fairly well correlated, the J_r distributions do not agree well.

4. Conclusions and Future Directions

Over the two storm intervals, the linear regression coefficients (C_L) between I_{Total} from all models and AMPERE are higher than 0.77 indicating that the models have predictive potential but the average ratio of I_{Total} ranges from 0.3 to 3.5 suggesting that the quantitative estimates may be substantially different from the natural system. Comparisons of the two-dimensional J_r patterns show that while yielding J_r broadly similar to AMPERE, they are substantially at variance with AMPERE in a number of ways. This is reflected in generally low C_L between J_r at a given time with the average C_L ranging from 0.10 to 0.29. The W05 model often yields currents that extend farther equatorward than observed, whereas the MHD models do not yield currents as low in MLAT as observed, often underestimating the equatorward extent by 10° to 15° MLAT. In addition, the latitudinal span of the currents in the models is about twice that from AMPERE. The MHD simulations do exhibit a variation of current patterns comparable to the AMPERE results, but the W05 statistical model yields less variation in the J_r patterns than observed. We note that empirical statistical models for Birkeland currents have also evolved markedly [e.g., *He et al*., 2012] and the availability of new data sets may allow improvements in the reliability of these models as well. Interestingly, even though only the SWMF included an inner magnetosphere module, it did not consistently yield clearer Region 2 sense currents than the LFM or OGGCM simulations. In any case, an inner magnetosphere module has been successfully coupled to the LFM code [*Pembroke et al*., 2012]. Finally, nightside currents often associated with substorm-like surges in nightside currents are not resolved in any of the models even though the total current in these systems can exceed several million amperes.

In general, the MHD codes reflected the dayside currents and the most poleward currents but did not typically represent the equatorward currents well and in particular did not capture the dynamics of the nightside currents. This suggests that the simulations are fairly good at reproducing the directly driven aspects of the currents resulting from magnetopause reconnection that correspond to the most poleward currents [e.g., *Cowley*, 2000]. The consistency of the Region 2 sense currents was not uniformly better between AMPERE and the SWMF results than with LFM and OGGCM even though only the SWMF simulations include ring current physics via the coupled Rice Convection Model [e.g., *Toffoletto et al.*, 2003]. This suggests that including a ring current module is not in itself a guarantee of dramatically superior representation of the Region 2 currents and that including other processes and technical advances also need to be pursued.

The SWPC challenge runs do not represent the most advanced codes [cf. *Raeder et al.*, 2010; *Welling et al.*, 2015a, 2015b; *Wiltberger et al.*, 2016], nor do they reflect the range of processes and implementations that have been studied. Indeed, considerable work has been done assessing how physical processes other than an inner magnetosphere ring current and other changes in the codes affect global simulation results. Increasing the simulation resolution leads to Birkeland currents with latitudinal extents comparable to those resolved by AMPERE, stronger Region 2 currents, and greater confinement of the convection potential to higher latitudes owing to the shielding effects of the Region 2 currents [cf. *Raeder et al.*, 2010; *Merkin et al.*, 2013; *Welling et al.*, 2015a, 2015b; *Wiltberger et al.*, 2016]. The relatively low Region 2 currents in all of the SWPC challenge runs and the broad latitude extent of the currents in the LFM and SWMF runs relative to AMPERE therefore suggest that higher resolution simulations are needed. Obtaining currents at latitudes as low as 50° MLAT requires simulations with inner boundaries not higher than ~2 R_E geocentric distance, corresponding to 45° MLAT, which the SWMF and LFM codes in the SWPC challenge events did. Thus, it seems that higher resolution is necessary to take full advantage of the additional degrees of freedom afforded by the low-altitude inner boundary.

The ionospheric conductance specification has traditionally been implemented via empirical parameterizations for precipitation and consequent ionization [cf. *Knight*, 1973; *Robinson et al.*, 1987; *Lyon et al.*, 2004], and alternate approaches to deriving or specifying the conductance distributions have also been studied [*Amm*, 2002; *Green et al.*, 2007; *McGranaghan et al.*, 2016]. The ionospheric conductivity has a significant influence on the MHD simulations not only in modifying the potential but also by regulating saturation effects and changing the geometry of the magnetosphere [cf. *Merkine et al.*, 2003; *Merkin et al.*, 2005b, 2005c]. The complex magnetosphere-ionosphere coupling results in behavior which is neither a constant voltage nor a constant current system [e.g., *Raeder et al.*, 2001; *Ridley et al.*, 2004]. Comparisons between simulations with an empirical ionosphere model and a coupled ionosphere/thermosphere model (TIE-GCM) yielded different conductivities but show little differences between the cross polar cap potential pattern during modest to strong driving conditions [*Wiltberger et al.*, 2004]. Including effects of anomalous electron heating, however, leads to substantial differences in the simulation results and improved agreement in the storm time polar cap potential and Birkeland currents with observations [*Merkin et al.*, 2005a]. Achieving improved quantitative agreement is therefore likely to require a nonlinear conductance representation representing the various sources of ionization and conductance [cf. *Ridley et al.*, 2004] and the effects of small-scale turbulence and electron heating in the ionosphere responsible for anomalous conductivity [*Dimant and Oppenheim*, 2011a, 2011b]. Finally, we note that inductive and altitude-dependent processes in the ionosphere that cannot be represented in terms of electrostatic solutions using height-integrated conductivities may also need to be considered [cf. *Amm et al.*, 2008].

The influence of ionospheric heavy ion outflow, principally O^+, has also been studied extensively [cf. *Kronberg et al.*, 2014; *Welling et al.*, 2015a; *Wiltberger*, 2015]. Heavy ion outflows from the ionosphere significantly modify magnetospheric dynamics [cf. *Winglee et al.*, 2002; *Brambles et al.*, 2010, 2011]. In particular, heavy ion outflows appear to slow magnetospheric convection leading to a reduction in Birkeland currents and polar cap potential [*García et al.*, 2010; *Welling and Zaharia*, 2012]. They also may lead to changes in the character of magnetotail reconnection dynamics [*Brambles et al.*, 2011; *Ouellette et al.*, 2013; *Wiltberger*, 2015], and interactions between outflows and the ring current appear to modify the Region 2 currents as well [*Welling et al.*, 2015b]. Thus, the effects of ionospheric ions may also need to be included to improve both the quantitative estimates for convection intensity and hence the Birkeland current.

n summary, there are various ways in which the simulations could be modified, all of which may improve the correspondence with the AMPERE observations. Since the inner boundary, ionospheric conductance, and heavy ion effects all depend on having sufficient resolution to yield the latitude structure and locations of the Birkeland currents, it would seem that using higher resolution while implementing coupling with inner magnetosphere models would be the first change to assess. Whether the remaining discrepancies indicate implementing improved conductance estimates, adding ionospheric ion outflows, or other physical processes currently omitted from the models would remain to be considered and could be studied by comparing results of suitably controlled numerical experiments. The dynamics of nightside currents, which were not captured in any of the simulations, may or may not emerge from these subsequent simulations. The breadth of challenges implies that considerable additional model development and validation comparison work remains. Given the challenges of predicting M-I dynamics and substorm occurrence in particular, developing and sustaining a real-time monitoring capability of high-latitude electrodynamics will likely remain important for the foreseeable future.

Acknowledgments
Support for AMPERE has been provided under NSF sponsorship under grants ATM-0739864 and AGS-1420184. B.J.A. thanks Daniel R. Weimer for helpful discussions guiding the use, evaluation, and comparison of the W05 results with AMPERE products. B.J.A. also thanks A. Pulkkinen for effective leadership of the LWS-GIC Institute efforts. All AMPERE data are available via http://ampere.jhuapl.edu. Simulation output in digital form are available via http://ccmc.gsfc.nasa.gov/challenges/dBdt/. The W05 code is available from Daniel J. Weimer (dweimer@vt.edu). Provisional auroral current data are available from the World Data Center for Geomagnetism at Kyoto University (http://wdc.kugi.kyoto-u.ac.jp/aedir/index.html).

References

Amm, O. (2002), Method of characteristics for calculating ionospheric electrodynamics from multisatellite and ground-based radar data, *J. Geophys. Res.*, *107*(A), 1270, doi:10.1029/2001JA005077.

Amm, O., A. Aruliah, S. C. Buchert, R. Fujii, J. W. Gjerloev, A. Ieda, T. Matsuo, C. Stolle, H. Vanhamäki, and A. Yoshikawa (2008), Towards understanding the electrodynamics of the 3-dimensional high-latitude ionosphere: Present and future, *Ann. Geophys.*, *26*(1), 3913–3932, doi:10.5194/angeo-26-3913-2008.

Anderson, B. J., T. A. Potemra, P. F. Bythrow, L. J. Zanetti, D. B. Holland, and J. D. Winningham (1993), Auroral currents during the magnetic storm of November 8 and 9, 1991: Observations from the Upper Atmosphere Research Satellite Particle Environment Monitor, *Geophys. Res. Lett.*, *20*, 1327–1330, doi:10.1029/93GL01106.

Anderson, B. J., K. Takahashi, and B. A. Toth (2000), Sensing global Birkeland currents with Iridium® engineering magnetometer data, *Geophys. Res. Lett.*, *27*, 4045–4048, doi:10.1029/2000GL000094.

Anderson, B. J., H. Korth, C. L. Waters, D. L. Green, and P. Stauning (2008), Statistical Birkeland current distributions from magnetic field observations by the Iridium constellation, *Ann. Geophys.*, *26*, 671–687, doi:10.5194/angeo-26-671-2008.

Anderson, B. J., H. Korth, C. L. Waters, D. L. Green, V. G. Merkin, R. J. Barnes, and L. P. Dryud (2014), Development of large-scale Birkeland currents determined from the Active Magnetosphere and Planetary Electrodynamics Response Experiment, *Geophys. Res. Lett.*, *41*, 3017–3025, doi:10.1002/2014GL059941.

Archer, M. O., T. S. Horbury, J. P. Eastwood, J. M. Weygand, and T. K. Yeoman (2013), Magnetospheric response to magnetosheath pressure pulses: A low-pass filter effect, *J. Geophys. Res. Space Physics*, *118*, 5454–5466, doi:10.1002/jgra.50519.

Brambles, O. J., W. Lotko, P. A. Damiano, B. Zhang, M. Wiltberger, and J. Lyon (2010), Effects of causally driven cusp O^+ outflow on the storm time magnetosphere-ionosphere system using a multifluid global simulation, *J. Geophys. Res.*, *115*, A00J04, doi:10.1029/2010JA015469.

Brambles, O. J., W. Lotko, B. Zhang, M. Wiltberger, J. Lyon, and R. J. Strangeway (2011), Magnetosphere sawtooth oscillations induced by ionospheric outflow, *Science*, *332*, 1183, doi:10.1126/science.1202869.

Clausen, L. B. N., J. B. H. Baker, J. M. Ruohoniemi, S. E. Milan, and B. J. Anderson (2012), Dynamics of the region 1 Birkeland current oval derived from the Active Magnetosphere and Planetary Electrodynamics Response Experiment (AMPERE), *J. Geophys. Res.*, *117*, A06233, doi:10.1029/2012JA017666.

Cosgrove, R. B., et al. (2014), Empirical model of Poynting flux derived from FAST data and a cusp signature, *J. Geophys. Res. Space Physics*, *119*, 411–430, doi:10.1002/2013JA019105.

Council, N. R. (2008), *Severe Space Weather Events—Understanding Societal and Economic Impacts: A Workshop Report*, The National Academies Press, Washington, DC.

Cowley, S. W. H. (2000), Magnetosphere-ionosphere interactions: A tutorial review, in *Magnetospheric Current Systems*, *Geophys. Monogr. Ser.*, vol. 118, edited by S. Ohtani et al., AGU, Washington, D. C.

Coxon, J. C., S. E. Milan, L. B. N. Clausen, B. J. Anderson, and H. Korth (2014), A superposed epoch analysis of the regions 1 and 2 Birkeland currents observed by AMPERE during substorms 2014, Development of large-scale Birkeland currents determined from the Active Magnetosphere and Planetary Electrodynamics Response Experiment, *J. Geophys. Res. Space Physics.*, *119*, 9834–9846, doi:10.1002/2014JA020500.

Curto, J., J. Castell, and F. Del Moral (2016), Sfe: Waiting for the big one, *J. Space Weather Space Clim.*, *6*, A23, doi:10.1051/swsc/2016018.

De Zeeuw, D. L., T. I. Gombosi, C. P. T. Groth, K. G. Powell, and Q. F. Stout (2000), An adaptive MHD method for global space weather simulations, *IEEE Trans. Plasma Sci.*, *28*, 1956–1965, doi:10.1109/27.902224.

De Zeeuw, D. L., S. Sazykin, R. A. Wolf, T. I. Gombosi, A. J. Ridley, and G. Tóth (2004), Coupling of a global MHD code and an inner magnetospheric model: Initial results, *J. Geophys. Res.*, *109*, A12219, doi:10.1029/2003JA010366.

DeJong, A. D., A. J. Ridley, X. Cai, and C. R. Clauer (2009), A statistical study of BRIs (SMCs), isolated substorms, and individual sawtooth injections, *J. Geophys. Res.*, *114*, A08215, doi:10.1029/2008JA013870.

Dimant, Y. S., and M. M. Oppenheim (2011a), Magnetosphere-ionosphere coupling through *E* region turbulence: 1. Energy budget, *J. Geophys. Res.*, *116*, A09303, doi:10.1029/2011JA016648.

Dimant, Y. S., and M. M. Oppenheim (2011b), Magnetosphere-ionosphere coupling through *E* region turbulence: 2. Anomalous conductivities and frictional heating, *J. Geophys. Res.*, *116*, A09304, doi:10.1029/2011JA016649.

Freeman, M. P., N. C. Freeman, and C. J. Farrugia (1995), A linear perturbation analysis of magnetopause motion in the Newton-Busemann limit, *Ann. Geophys.*, *13*, 907–918, doi:10.1007/s00585-995-0907-0.

García, K. S., V. G. Merkin, and W. J. Hughes (2010), Effects of nightside O^+ outflow on magnetospheric dynamics: Results of multifluid MHD modeling, *J. Geophys. Res.*, *115*, A00J09, doi:10.1029/2010JA015730.

Glocer, A., G. Tóth, Y. J. Ma, T. Gombosi, J.-C. Zhang, and L. M. Kistler (2009), Multi-fluid BATS-R-US: Magnetospheric composition and dynamics during geomagnetic storms, initial results, *J. Geophys. Res.*, *114*, A12203, doi:10.1029/2009JA014418.

Green, D. L., C. L. Waters, H. Korth, B. J. Anderson, A. J. Ridley, and R. J. Barnes (2007), Technique: Large-scale ionospheric conductance estimated from combined satellite and ground-based electromagnetic data, *J. Geophys. Res.*, *112*(A5, A05303), doi:10.1029/2006JA012069.

He, M., J. Vogt, H. Luhr, E. Sorbalo, A. Blagau, G. Le, and G. Lu (2012), A high-resolution model of field-aligned currents through empirical orthogonal functions analysis (MFACE), *Geophys. Res. Lett.*, *39*, L18105, doi:10.1029/2012GL053168.

Kleiber, W., B. Hendershott, S. R. Sain, and M. Wiltberger (2016), Feature-based validation of the Lyon-Fedder-Mobarry magnetohydrodynamical model, *J. Geophys. Res. Space Physics*, *121*, 1192–1200, doi:10.1002/2015JA021825.

Knight, S. (1973), Parallel electric fields, *Planet. Space Sci.*, *21*, 741–750.

Korth, H., B. J. Anderson, H. Frey, and C. L. Waters (2005), High-latitude electromagnetic and particle energy flux during an event with sustained strongly northward IMF, *Ann. Geophys.*, *23*, 1295–1310, doi:10.5194/angeo-23-1295-2005.

Korth, H., B. J. Anderson, J. M. Ruohoniemi, H. U. Frey, C. L. Waters, T. J. Immel, and D. L. Green (2008), Global observations of electromagnetic and particle energy flux for an event during northern winter with southward interplanetary magnetic field, *Ann. Geophys.*, *26*, 1415–1430, doi:10.5194/angeo-26-1415-2008.

Korth, H., B. J. Anderson, and C. L. Waters (2010), Statistical analysis of the dependence of large-scale Birkeland currents on solar wind parameters, *Ann. Geophys.*, *28*, 515–530.

Kronberg, E. A., et al. (2014), Circulation of heavy ions and their dynamical effects in the magnetosphere: Recent observations and models, *Space Sci. Rev.*, *184*, 173–235, doi:10.1007/s11214-014-0104-0.

Love, J. J., E. J. Rigler, A. Pulkkinen, and P. Riley (2015), On the lognormality of historical magnetic storm intensity statistics: Implications for extreme-event probabilities, *Geophys. Res. Lett.*, *42*, 6544–6553, doi:10.1002/2015GL064842.

Lu, G., M. E. Hagan, K. Häusler, E. Doornbos, S. Bruinsma, B. J. Anderson, and H. Korth (2014), Global ionospheric and thermospheric response to the 5 April 2010 geomagnetic storm: An integrated data-model investigation, *J. Geophys. Res. Space Physics*, *119*, 10,358–10,375, doi:10.1002/2014JA020555.

Lyatskaya, S., W. Lyatsky, and G. V. Khazanov (2014), Effect of interhemispheric field-aligned currents on Region-1 currents, *Geophys. Res. Lett.*, *41*, 3731–3737, doi:10.1002/2014GL060413.

Lyon, J. G., J. A. Fedder, and C. M. Mobarry (2004), The Lyon-Fedder-Mobarry (LFM) global MHD magnetospheric simulation code, *J. Atmos. Sol. Terr. Phys.*, *66*, 1333–1350, doi:10.1016/j.jastp.2004.03.020.

Lyons, L. R., et al. (2016), 2013 March 17 storm: Synergy of observations related to electric field modes and their ionospheric and magnetospheric effects, *J. Geophys. Res. Space Physics*, *121*, 10,880–10,897, doi:10.1002/2016JA023237.

Marsal, S., A. D. Richmond, A. Maute, and B. J. Anderson (2012), Forcing the TIEGCM model with Birkeland currents from the Active Magnetosphere and Planetary Electrodynamics Response Experiment, *J. Geophys. Res.*, *117*, A06308, doi:10.1029/2011JA017416.

Matsuo, T., D. J. Knipp, A. D. Richmond, L. Kilcommons, and B. J. Anderson (2015), Inverse procedure for high-latitude ionospheric electrodynamics: Analysis of satellite-borne magnetometer data, *J. Geophys. Res. Space Physics*, *120*, 5241–5251, doi:10.1002/2014JA020565.

McComas, D. J., S. J. Bame, P. L. Barker, W. C. Feldman, J. L. Phillips, P. Riley, and J. W. Griffee (1998), Solar Wind Electron Proton Alpha Monitor (SWEPAM) for the Advanced Composition Explorer, *Space Sci. Rev.*, *86*, 563–612.

McGranaghan, R., D. J. Knipp, T. Matsuo, and E. Cousins (2016), Optimal interpolation analysis of high-latitude ionospheric Hall and Pedersen conductivities: Application to assimilative ionospheric electrodynamics reconstruction, *J. Geophys. Res. Space Physics*, *121*, 4898–4923, doi:10.1002/2016JA022486.

Merkin, V. G., and J. G. Lyon (2010), Effects of the low-latitude ionospheric boundary condition on the global magnetosphere, *J. Geophys. Res.*, *115*, A10202, doi:10.1029/2010JA015461.

Merkin, V. G., G. Milikh, K. Papadopoulos, J. Lyon, Y. S. Dimant, A. S. Sharma, C. Goodrich, and M. Wiltberger (2005a), Effect of anomalous electron heating on the transpolar potential in the LFM global MHD model, *Geophys. Res. Lett.*, *32*, L22101, doi:10.1029/2005GL023315.

Merkin, V. G., A. S. Sharma, K. Papadopoulos, G. Milikh, J. Lyon, and C. Goodrich (2005b), Global MHD simulations of the strongly driven magnetosphere: Modeling of the transpolar potential saturation, *J. Geophys. Res.*, *110*, A09203, doi:10.1029/2004JA010993.

Merkin, V. G., A. S. Sharma, K. Papadopoulos, G. Milikh, J. Lyon, and C. Goodrich (2005c), Relationship between the ionospheric conductance, field aligned current, and magnetopause geometry: Global MHD simulations, *Planet. Space Sci.*, *53*, 873, doi:10.1016/j.pss.2005.04.001.

Merkin, V. G., B. J. Anderson, J. G. Lyon, H. Korth, M. Wiltberger, and T. Motoba (2013), Global evolution of Birkeland currents on 10-min time scales: MHD simulations and observations, *J. Geophys. Res. Space Physics*, *118*, 4977–4997, doi:10.1002/jgra.50466.

Merkine, V. G., K. Papadopoulos, G. Milikh, A. S. Sharma, X. Shao, J. Lyon, and C. Goodrich (2003), Effects of the solar wind electric field and ionospheric conductance on the cross polar cap potential: Results of global MHD modeling, *Geophys. Res. Lett.*, *30*(23), 2180, doi:10.1029/2003GL017903.

Muhlbacher, S., C. J. Farrugia, J. Raeder, H. K. Biernat, and R. B. Torbert (2005), A statistical investigation of dayside erosion showing saturation response, *J. Geophys. Res.*, *110*, A11207, doi:10.1029/2005JA011177.

Murr, D. L., and W. J. Hughes (2007), The coherence between the IMF and high-latitude ionospheric flows: The dayside magnetosphere-ionosphere low-pass filter, *J. Atmos. Sol. Terr. Phys.*, *69*, 223–233, doi:10.1016/j.jastp.2006.07.019.

National Science and Technology Council (2015a), National Space Weather Strategy, Executive Office of the President (EOP), USA. [Available at https://whitehouse.gov/sites/default/files/microsites/ostp/final_nationalspaceweatherstrategy_20151028.pdf.]

National Science and Technology Council (2015b), National Space Weather Action Plan, Executive Office of the President (EOP), USA. [Available at https://www.whitehouse.gov/sites/default/files/microsites/ostp/final_nationalspaceweatheractionplan_20151028.pdf.]

Ngwira, C. M., A. Pulkkinen, M. M. Kuznetsova, and A. Glocer (2014), Modeling extreme "Carrington-type" space weather events using three-dimensional global MHD simulations, *J. Geophys. Res. Space Physics*, *119*, 4456–4474, doi:10.1002/2013JA019661.

North American Electric Reliability Corporation GMD Task Force (2012), 2012 Special Reliability Assessment Interim Report: Effects of geomagnetic disturbances on the bulk power system, NERC, February 2012.

Ohtani, S., H. Korth, S. Wing, E. R. Talaat, H. U. Frey, and J. W. Gjerloev (2012), The double auroral oval in the dusk-midnight sector: Formation, mapping and dynamics, *J. Geophys. Res.*, *117*, A08203, doi:10.1029/2011JA017501.

Ouellette, J. E., O. J. Brambles, J. G. Lyon, W. Lotko, and B. N. Rogers (2013), Properties of outflow-driven sawtooth substorms, *J. Geophys. Res. Space Physics*, *118*, 3223–3232, doi:10.1002/jgra.50309.

Partamies, N., T. I. Pulkkinen, R. L. McPherron, K. McWilliams, C. R. Bryant, E. Tanskanen, H. J. Singer, G. D. Reeves, and M. F. Thomsen (2009), Different magnetospheric modes: Solar wind driving and coupling efficiency, *Ann. Geophys.*, *27*, 4281–4291, doi:10.5194/angeo-27-4281-2009.

Pembroke, A., F. Toffoletto, S. Sazykin, M. Wiltberger, J. Lyon, V. Merkin, and P. Schmitt (2012), Initial results from a dynamic coupled magnetosphere-ionosphere-ring current model, *J. Geophys. Res.*, *117*, A02211, doi:10.1029/2011JA016979.

Powell, K. G., P. L. Roe, T. J. Linde, T. I. Gombosi, and D. L. De Zeeuw (1999), A solution-adaptive upwind scheme for ideal magnetohydrodynamics, *J. Comput. Phys.*, *154*, 284–309, doi:10.1006/jcph.1999.6299.

Pulkkinen, A. A., et al. (2017), Geomagnetically induced currents: Science, engineering and applications readiness, *Space Weather*, *15*, doi:10.1002/2016SW001501.

Pulkkinen, A., et al. (2013), Community-wide validation of geospace model ground magnetic field perturbation predictions to support model transition to operations, *Space Weather*, *11*, 369–385, doi:10.1002/swe.20056.

Raeder, J., Y. L. Wang, and T. J. Fuller-Rowell (2001), Geomagnetic storm simulation with a coupled magnetosphere-ionosphere-thermosphere model, in *Space Weather*, *AGU Geophys. Monogr. Ser.*, vol. 125, pp. 377, AGU, Washington, D. C.

Raeder, J., D. Larson, W. Li, E. L. Kepko, and T. Fuller-Rowell (2008), OpenGGCM simulations for the THEMIS mission, *Space Sci. Rev.*, *141*, 535, doi:10.1007/s1121400894215.

Raeder, J., P. Zhu, Y. Ge, and G. L. Siscoe (2010), OpenGGCM simulation of a substorm: Axial tail instability and ballooning mode preceding substorm onset, *J. Geophys. Res.*, *115*, A00I16, doi:10.1029/2010JA015876.

Ridley, A. J., D. L. De Zeeuw, T. I. Gombosi, and K. G. Powell (2001), Using steady state MHD results to predict the global state of the magnetosphere-ionosphere system, *J. Geophys. Res.*, *106*, 30,067–30,076, doi:10.1029/2000JA002233.

Ridley, A. J., K. C. Hansen, G. Tóth, D. L. De Zueew, T. I. Gombosi, and K. G. Powell (2002), University of Michigan MHD results of the GGCM metrics challenge, *J. Geophys. Res.*, *107*(A10), 1290, doi:10.1029/2001JA000253.

Ridley, A. J., T. I. Gombosi, and D. L. Zeeuw (2004), Ionospheric control of the magnetosphere: Conductance, *Ann. Geophys.*, *22*, 567–584, doi:10.5194/angeo-22-567-2004.

Robinson, R. M., R. R. Vondrak, K. Miller, T. Dabbs, and D. Hardy (1987), On calculating ionospheric conductances from the flux and energy of precipitating electrons, *J. Geophys. Res.*, *92*, 2565–2569, doi:10.1029/JA092iA03p02565.

Siscoe, G., J. Raeder, and A. Ridley (2004), Transpolar potential saturation models compared, *J. Geophys. Res.*, *109*, A09203, doi:10.1029/2003JA010318.

Smith, C. W., J. L'Heureux, N. F. Ness, M. H. Acuña, L. F. Burlaga, and J. Scheifele (1998), The ACE Magnetic Fields Experiment, *Space Sci. Rev.*, *86*, 613–632.

Toffoletto, F. R., S. Sazykin, R. W. Spiro, and R. A. Wolf (2003), Inner magnetospheric modeling with the Rice Convection Model, *Space Sci. Rev.*, *107*, 175–193.

Tóth, G., et al. (2005), Space weather modeling framework: A new tool for the space science community, *J. Geophys. Res.*, *110*, A12226, doi:10.1029/2005JA011126.

Tóth, G., et al. (2012), Adaptive numerical algorithms in space weather modeling, *J. Comp. Phys.*, *231*, 870–903, doi:10.1016/j.jcp.2011.02.006.

Tsurutani, B. T., and G. S. Lakhina (2014), An extreme coronal mass ejection and consequences for the magnetosphere and Earth, *Geophys. Res. Lett.*, *41*, 287–292, doi:10.1002/2013GL058825.

Waters, C. L., B. J. Anderson, and K. Liou (2001), Estimation of global field aligned currents using Iridium magnetometer data, *Geophys. Res. Lett.*, *28*, 2165–2168, doi:10.1029/2000GL012725.

Weimer, D. R. (2005a), Improved ionospheric electrodynamic models and application to calculating Joule heating rates, *J. Geophys. Res.*, *110*, A05306, doi:10.1029/2004JA010884.

Weimer, D. R. (2005b), Predicting surface geomagnetic variations using ionospheric electrodynamic models, *J. Geophys. Res.*, *110*, A12307, doi:10.1029/2005JA011270.

Welling, D. T., and S. G. Zaharia (2012), Ionospheric outflow and cross polar cap potential: What is the role of magnetospheric inflation?, *Geophys. Res. Lett.*, *39*, L23101, doi:10.1029/2012GL054228.

Welling, D. T., et al. (2015a), The Earth: Plasma sources, losses, and transport processes, *Space Sci. Rev.*, *192*, 145–208, doi:10.1007/s11214-015-0187-2.

Welling, D. T., V. K. Jordanova, A. Glocer, G. Toth, M. W. Liemohn, and D. R. Weimer (2015b), The two-way relationship between ionospheric outflow and the ring current, *J. Geophys. Res. Space Physics*, *120*, 4338–4353, doi:10.1002/2015JA021231.

Welling, D. T., B. J. Anderson, G. Crowley, A. A. Pulkkinen, and L. Rastaetter (2016), Exploring predictive performance: A reanalysis of the geospace model transition challenge, *Space Weather*, *14*, doi:10.1002/2016SW001505.

Wilder, F. D., G. Crowley, B. J. Anderson, and A. D. Richmond (2012), Intense dayside Joule heating during the 5 April 2010 geomagnetic storm recovery phase observed by AMIE and AMPERE, *J. Geophys. Res.*, *117*, A05207, doi:10.1029/2011JA017262.

Wiltberger, M. (2015), Review of global simulation studies of effect of ionospheric outflow on magnetosphere-ionosphere system dynamics, in *Magnetotails in the Solar System*, pp. 373–392, John Wiley, Hoboken, New Jersey, doi:10.1002/978111884232.

Wiltberger, M., W. Wang, A. G. Burns, S. C. Solomon, J. G. Lyon, and C. C. Goodrich (2004), Initial results from the coupled magnetosphere ionosphere thermosphere model: Magnetospheric and ionospheric responses, *J. Atmos. Sol. Terr. Phys.*, *66*(1), 1411–1423, doi:10.1016/j.jastp.2004.03.026.

Wiltberger, M., W. Lotko, J. G. Lyon, P. Damiano, and V. Merkin (2010), Influence of cusp O^+ outflow on magnetotail dynamics in a multifluid MHD model of the magnetosphere, *J. Geophys. Res.*, *115*, A00J05, doi:10.1029/2010JA015579.

Wiltberger, M., E. J. Rigler, V. Merkin, and J. G. Lyon (2016), Structure of high latitude currents in magnetosphere-ionosphere models, *Space Sci. Rev.*, 1–24, doi:10.1007/s11214-016-0271-2.

Wiltberger, M., E. J. Rigler, V. Merkin, and J. G. Lyon (2016), Structure of high latitude currents in magnetosphere-ionosphere models, *Space Sci. Rev.*, *1–41*, doi:10.1007/s11214-016-0271-2.

Winglee, R. M., D. Chua, M. Brittnacher, G. K. Parks, and G. Lu (2002), Global impact of ionospheric outflows on the dynamics of the magnetosphere and cross-polar cap potential, *J. Geophys. Res.*, *107*(A9), 1237, doi:10.1029/2001JA000214.

Yu, Y., and A. J. Ridley (2008), Validation of the Space Weather Modeling Framework using ground-based magnetometers, *Space Weather*, *6*, S05002, doi:10.1029/2007SW000345.